PCCP

Physical Chemistry Chemical Physics

This article can be cited before page numbers have been issued, to do this please use: S. Rahane, G. K. Rahane, Y. Jadhav, M. P. Nasane, H. I. Eya, D. Kalleshappa, K. Hareesh, J. Pawar, S. R. Jadkar and N. Y. Y. Dzade, *Phys. Chem. Chem. Phys.*, 2025, DOI: 10.1039/D5CP02259B.


Volume 19
Number 1
7 January 2017
Pages 1-896

PCCP
Physical Chemistry Chemical Physics
rsc.li/pccp

ISSN 1463-9076

ROYAL SOCIETY OF CHEMISTRY

PAPER
H.-P. Loock *et al.*
Determination of the thermal, oxidative and photochemical degradation rates of scintillator liquid by fluorescence EEM spectroscopy

ROYAL SOCIETY OF CHEMISTRY

rsc.li/pccp

View Article Online
DOI: 10.1039/D5CP02259B

Exploring $Cs_2AgIn_xBi_{1-x}Cl_6$ Double Perovskites for Optoelectronics: Insights from Theoretical and Photophysical Approach

Swati N. Rahane,[a] Ganesh K. Rahane,[b] Yogesh Jadhav,[c] Mamta P. Nasane[d], Henry I. Eya[f], Deepak Kalleshappa[d], Hareesh K.[b], Jayant Pawar[e], Sandesh R. Jadkar,[a] and Nelson Y. Dzade,*[f]*

[a]*Department of Physics, Savitribai Phule Pune University, Pune 411007, India.*
[b]*Department of Physics, Manipal Institute of Technology Bengaluru, Manipal Academy of Higher Education, Manipal 576104, India*
[c]*BacPlexTechnologies Private Limited, C/O AIC IISER PUNE SEED FOUNDATION*
IISER Pune Campus, Dr. Homi Bhabha Road, Pashan, Pune 411008, Maharashtra, India
[d]*Reva University, Yelahanka, Bengaluru Karnataka IN 560064*
[e]*Krishna Vishwa Vidyapeeth (Deemed to be University), Malkapur, Karad -415539, Maharashtra*
[f]*Department of Energy and Mineral Engineering, Pennsylvania State University, University Park, PA 16802, United States*

Nelson Y. Dzade* - Email: nxd5313@psu.edu
Sandesh R. Jadkar* - Email: sandesh@physics.unipune.ac.in

Abstract

Lead-free halide double perovskites (HDPs) have become attractive materials for optoelectronic applications owing to their nontoxicity, structural stability, and germane photoelectric properties. In this work, we report the synthesis of high-quality In-alloyed $Cs_2AgIn_xBi_{1-x}Cl_6$ nanocrystals (NCs) using the antisolvent recrystallization method and comprehensively investigate the effects of In alloying on the structural, morphological, optoelectronic, and temperature-dependent photoluminescence (TDPL) properties, using the state-of-the-art experimental and computational tools. Both XRD and Raman spectroscopy analyses confirmed the synthesis of highly crystalline $Cs_2AgIn_xBi_{1-x}Cl_6$ materials, which exhibit cubic morphology, as confirmed from TEM analysis. Room temperature photoluminescence (PL) measurements reveal a drastic increase in the intensity above 75% In concentration with dual emission, whereas the time-resolved PL (TRPL) results show an increase in the average lifetime values with an increase in In content, suggesting that the materials have excellent optical properties and hence are suitable candidates for optoelectronics. The TDPL measurements yield the smallest Huang-Rhys factor (18.6) for the $Cs_2AgIn_xBi_{(1-x)}Cl_6$ (x = 0.9) sample, indicating weak exciton-phonon coupling in this composition. When deployed

View Article Online
DOI: 10.1039/D5CP02259B

in the fabrication of a photodetector device, the $Cs_2AgIn_xBi_{(1-x)}Cl_6$ (x=0.9) sample exhibits significantly enhanced photoresponsivity and faster response time, confirming its potential for photodetector applications. Complementary DFT calculations show that In alloying modifies the band structure of $Cs_2AgIn_xBi_{(1-x)}Cl_6$. Our results provide valuable insights into designing multifunctional $Cs_2AgIn_xBi_{(1-x)}Cl_6$-based materials for next-generation energy and optoelectronic devices.

Keywords: Exciton phonon coupling, Halide double perovskites, Nanocrystals, Optoelectronics

1. Introduction

Metal halide perovskites (MHPs) have emerged as a promising class of perovskites for cost-effective and high-performance applications in solar cells, light-emitting diodes (LEDs), and displays. [1-3] These perovskites demonstrate high optical absorption coefficients, significant PL quantum yield (PLQY), and easily tunable band gaps. [4-10] Moreover, they possess higher carrier lifetimes and diffusion lengths of charge carriers. [11,12] Such significant attributes render halide perovskites highly intriguing and suggest potential superiority over traditional optoelectronic devices. Their superior performance is primarily ascribed to their direct band gap and three-dimensional (3D) structure. [13] Altering the dimensions of MHPs from 3D to zero-dimensional (0D) by adjusting the A-site cation's size is feasible. However, the lower-dimensional perovskites currently trail behind their 3D counterparts in solar cell applications due to their limited light-harvesting capabilities. [14,15]

Understanding the optical properties and band structure of a semiconductor is vital for designing and developing efficient optoelectronic devices, as the band gap directly determines a material's ability to absorb and emit light, influencing the overall functionality of these devices. Recent studies have focused on all-inorganic lead halide perovskite nanocrystals ($CsPbX_3$, X = Cl, Br, I). These perovskites possess a unique three-dimensional structure and a direct band gap, resulting in a high absorption coefficient, low trap-state density, and near-unity photoluminescence quantum efficiency (PLQE), which makes them promising for optoelectronic applications. [16-19] Despite their promising attributes, the lead halide perovskites face toxicity and stability issues. Efforts are made to develop lead-free alternatives with exceptional environmental stability. In this

View Article Online
DOI: 10.1039/D5CP02259B

perspective, some progress has been made with Bi^{3+}, Sb^{3+}, and DP NCs. [20-30] These lead-free perovskites show an indirect band gap, leading to lower performance.

Recently, a novel lead-free $Cs_2AgInCl_6$ double perovskite (DP) possessing a band gap of 3.5 eV has been introduced. [31-34] This material features a direct band gap, with absorption occurring between the ultraviolet (UV) and visible spectrum. [31] In contrast, $Cs_2AgBiCl_6$ exhibits an indirect band gap of approximately 2.7-2.8 eV. Essentially, $Cs_2AgInCl_6$ demonstrates a direct transition with a wider band gap, while $Cs_2AgBiCl_6$ showcases an indirect transition with a relatively narrower band gap. [35] Designing the DP systems to converge indirect to direct transitions by adjusting the composition could yield materials with intermediate band gaps and enhanced optical properties, making them attractive for wide range of applications. These multifunctional properties have sparked recent interest in semiconductors for more versatile high-performance optoelectronic applications. [36-38]

While the optical properties have been studied in detail for the end members of the $Cs_2AgIn_xBi_{1-x}Cl_6$ family through TDPL measurements, other important properties like intrinsic defects, self-trapping, recombination rates, and the application in the field of optoelectronics have not been thoroughly studied for the compositional materials. A comprehensive approach combining experimental techniques, DFT, and advanced characterizations is essential to better understand the physical processes, such as defect states and band gap tunability. In this study, we systematically investigated the $Cs_2AgIn_xBi_{(1-x)}Cl_6$ materials to determine the impact of chemical changes on structural, optical, and electronic properties of these DP materials. Raman spectroscopy analysis provides insights into the local distortions, as well as the active vibrational modes present in the materials. These highly stable DPs exhibit emission in the visible region, which may be related to defect levels and surface traps. X-ray diffraction (XRD) analysis verified that all synthesized materials crystallize in the cubic phase. Results from energy dispersive spectroscopy (EDS) indicated a proportional rise in the atomic composition of In with an increase in In content, consistent with stoichiometry. We employed TDPL to probe the excitonic and defect states, and electrochemistry to assess charge transport. As the energy band alignment and band offset control charge transport and separation across the perovskite interface, we have employed electrochemical

View Article Online
DOI: 10.1039/D5CP02259B

cyclic voltammetry (CV) measurements to determine the band edge positions, specifically the valence band maximum (VBM) and conduction band minimum (CBM). The results showed prominent peaks, which are correlated with electron transfer from the valence band to the conduction band edges. Additionally, first-principles DFT calculations were used to gain insights into the electronic structure of these DPs. Beyond fundamental understanding, we demonstrate the potential of these materials for photodetector applications. This multidisciplinary approach not only advances our understanding of perovskite materials but also provides strategic insights for optimizing their functionality in real-world applications. These materials hold significant promise for applications in optoelectronics as well as photocatalysis, making them strong candidates for advancements in these fields.

2. Experimental Section/Methods

Materials

CsCl (TCI, 99%), AgCl (Sigma Aldrich 99.99%), $BiCl_3$ (HPLC, 92%), $InCl_3$ (TCI, 99.99%), isopropanol (IPA, AR Grade, 99.5%), dimethyl sulfoxide (DMSO, AR Grade, 99.5 %), Tetrabutyl ammonium perchlorate (TBAP-99.8%), toluene (AR grade, HPLC, 99.5%). The materials were used directly as received.

Synthesis of $Cs_2AgIn_xBi_{1-x}X_6$ (x = 0, 0.1, 0.25, 0.5, 0.75, 0.9, 1.0)

To synthesize the $Cs_2AgIn_xBi_{1-x}Cl_6$ (x=0) NCs, CsCl, AgCl, and $BiCl_3$ metal salts were dissolved in DMSO in the ratio of 2:1:1 to form a precursor solution. Typically, 0.2 mmol CsCl (33.7 mg), 0.1 mmol AgCl (14.3 mg), and 0.1 mmol $BiCl_3$ (31.5 mg) were dissolved in 5 mL DMSO to prepare a precursor solution. Next, 100 µL of this solution was added dropwise to 5 mL of IPA with vigorous stirring. The resulting solution is then centrifuged at 4500 rpm for 5 minutes to remove large crystals, followed by washing the obtained product three times to eliminate byproducts. The synthesis procedure for $Cs_2AgIn_xBi_{1-x}Cl_6$ (x=1) NCs mirrored that of $Cs_2AgIn_xBi_{1-x}Cl_6$ (x=0) NCs. For $Cs_2AgIn_xBi_{1-x}Cl_6$ (x=1) NCs, 0.2 mmol CsCl, 0.1 mmol AgCl, and 0.1 mmol $InCl_3$ were mixed in 5 mL DMSO to prepare a precursor solution, followed by dropwise addition of 100 µL of the precursor solution to 5 mL of IPA under vigorous stirring. This solution is centrifuged at 4500 rpm for 5 minutes and washed subsequently. A similar approach was employed for synthesizing $Cs_2AgIn_xBi_{1-x}X_6$ (x= 0.10, 0.25, 0.50, 0.75, and 0.90) NCs, with varying amounts of CsCl, AgCl, $BiCl_3$, and $InCl_3$ used to form precursors for injection.

View Article Online
DOI: 10.1039/D5CP02259B

Fabrication of the Photodetector Device

Fluorine-doped tin oxide (FTO) was used as the substrate for fabricating the photodetector device. Initially, the substrates were cleaned by sequential sonication in isopropyl alcohol, double-distilled water, and acetone for 15 minutes. Following the cleaning process, a compact TiO_2 (c-TiO_2) layer was deposited onto the FTO substrates using radio frequency (RF) sputtering, serving as the electron transport layer (ETL). Subsequently, the active material was deposited onto the TiO_2-coated FTO substrate via a simple drop-casting method. Finally, the cathode contact was given using graphite paste to form an FTO/c-TiO_2/$Cs_2AgIn_xBi_{(1-x)}Cl_6$/graphite photodetector device. For the top electrode contact, a graphite paste was prepared by mixing graphite powder in an IPA solution, and then it was deposited on FTO/c-TiO2/$Cs_2AgIn_xBi_{(1-x)}Cl_6$.

Characterizations of $Cs_2AgIn_xBi_{1-x}Cl_6$

XRD analysis is carried out utilizing a Bruker HR-XRD D8 Adv. instrument Cu-Kα radiation at 1.542 Å to generate diffraction patterns. Raman measurements were performed using a Renishaw InVia Raman microscope. The excitation wavelength of 532 nm was used as a source. UV/visible spectra are collected in DRS mode with a JASCO V-670 UV−visible Spectrophotometer. High-resolution imaging is performed using an aberration-corrected TEM in HR-TEM mode (ThermoFisher Tecnai T-20 ST) operated at 200 kV. The surface morphology and shape of the $Cs_2AgIn_xBi_{(1-x)}Cl_6$ DPs are examined through FE-SEM. Compositional analysis is conducted using EDS with a Bruker X Flash 6130 instrument. A PHI 5000 VERSA PROBE III ULVAC PHI instrument (Physical Electronics, USA) is used for XPS employing monochromatic AlK_α radiation at 1486.6 eV. The XPS chamber maintains a base vacuum level above 10^{-9} torr. Room temperature PL is recorded utilizing a Fluorolog Horiba scientific setup, while the TDPL measurements employ the JANIS (model no. VNF-10) PL setup. Time-resolved photoluminescence (TRPL) is recorded using the Horiba Jobin Yvon Fluorocube-01-NL fluorescence lifetime system, equipped with a picosecond 405 nm laser diode source that can generate pulse widths shorter than 70 ps. Data analysis is carried out using Horiba data station software. The Metrohm Potentiostat/Galvanostat Autolab PGSTAT 302N is implemented for CV measurements. The standard three-electrode system is used to record CV as per our previous report. [39-42] The working electrode was made from

View Article Online
DOI: 10.1039/D5CP02259B

glassy carbon, and a silver wire and platinum were used as a reference and counter electrode, respectively. The measurements were performed in a 15 mL solution of dichloromethane (DCM) containing 100 mM tetrabutylammonium perchlorate (TBAP) as the supporting electrolyte, all under inert nitrogen conditions. Before conducting CV measurements, the glassy carbon electrode is polished using alumina powder (0.5 μm), while the Ag/Pt electrodes are cleaned with dilute nitric acid and then rinsed with deionized water. Photo response measurements of the $Cs_2AgIn_xBi_{(1-x)}Cl_6$ double perovskite devices were recorded using a Keithley 2450 source meter connected to a computer. Light illumination was incident through an ORIEL SOL 2A 94022A Class ABA simulator. *I–V* characteristics were measured at a power density of 30 mW/cm^2 on an active layer with an area of 1.5*1.5 cm^2.

First-principles DFT characterization details

The first-principles DFT calculations were performed using the Vienna Ab initio Simulation Package (VASP).[43] First, we obtained the crystallographic files (CIFs) of $Cs_2AgIn_xBi_{(1-x)}Cl_6$ (x=0) and $Cs_2AgIn_xBi_{(1-x)}Cl_6$ (x=1) from the Materials Project database and performed geometric optimization using the generalized gradient approximation (GGA) Perdew-Burke-Ernzerhof (PBE) functional.[44] The ion core and valence electron wavefunctions were described using the Projector Augmented Wavefunction (PAW) pseudopotentials,[45] and a plane-wave energy cut-off of 600 eV was employed to converge the total energy of the structures within 10^{-7} eV and the residual forces on all relaxed atoms to 10^{-3} $eVÅ^{-1}$. The Brillouin zone was sampled using a 3 × 3 × 3 Monkhorst−Pack k-point mesh.[46] Furthermore, we accounted for vdW interactions in our calculations using the Grimme (DFT-D3) method.[47] Considering that the PBE functional underestimates the band gap of semiconductors, we employed the Hartree–Fock screened hybrid functional (HSE06) for the electronic and optical property calculations. Hartree–Fock exchange fractions of 25% and 40% were employed for $Cs_2AgIn_xBi_{(1-x)}Cl_6$ (x=0) and $Cs_2AgIn_xBi_{(1-x)}Cl_6$ (x=1), respectively, as they could predict the band gaps of the respective materials close to their experimental values. A higher k-point mesh of 5 × 5 × 5 was used for the density of state (DOS) and optical property calculations. The projected density of states (PDOS) and band structures were

View Article Online
DOI: 10.1039/D5CP02259B

plotted using SUMO software.[48] The linear optical properties of the materials were determined from the frequency-dependent complex dielectric function $\varepsilon(w)$, which is expressed as follows:

$$\varepsilon(w) = \varepsilon_1(w) + i\varepsilon_2(w), \tag{1}$$

where $\varepsilon_1(w)$ and $\varepsilon_2(w)$ are the real and imaginary parts of the dielectric function, respectively, and w is the frequency of photon. The frequency-dependent linear optical spectra, including the absorption coefficient $\alpha(w)$, refractive index $n(w)$, and reflectivity $R(w)$, were obtained from ε_1 (w) and $\varepsilon_2(w)$ as follows: [49-50]

$$\alpha(w) = \frac{\sqrt{2}\,w}{c}\left[\sqrt{\varepsilon_1^2 + \varepsilon_2^2} - \varepsilon_1\right]^{\frac{1}{2}} \tag{2}$$

$$n(w) = \left[\frac{\sqrt{\varepsilon_1^2+\varepsilon_2^2}+\varepsilon_1}{2}\right]^{\frac{1}{2}} \tag{3}$$

$$R(w) = \frac{(n-1)^2 + k^2}{(n+1)^2 + k^2} \tag{4}$$

where, c is the speed of light in a vacuum. These optical properties were extracted using VASPKIT.[49]

3. RESULTS AND DISCUSSION

3.1. Structural properties of $Cs_2AgIn_xBi_{1-x}Cl_6$ DPs

3.1.1. XRD Analysis

The $Cs_2AgIn_xBi_{1-x}Cl_6$ (x = 0.0, 0.1, 0.25, 0.5, 0.75, 0.9, 1.0) NCs were synthesized via the antisolvent recrystallization method. [25,28] The stoichiometry of In/Bi was varied to prepare the In alloyed $Cs_2AgIn_xBi_{1-x}Cl_6$ NCs. The XRD patterns for all these DPs are depicted in Figure 1(a). XRD analysis confirmed the high crystallinity of the synthesized materials, with all NCs adopting the $Fm\bar{3}m$ cubic space group like $Cs_2AgIn_xBi_{1-x}Cl_6$ (x=0) DPs. [28] We observe a monotonic shift in XRD peaks towards higher angles with an increase in In content, as can be seen for the peak at around 34° (Figure 1(b)), indicating lattice contraction due to the replacement of larger Bi^{3+} (ionic radius 117 pm) with the smaller In^{3+} (94 pm). Figure S1 in the Supporting Information represents the Williamson-Hall (W-H) plots for $Cs_2AgIn_xBi_{1-x}Cl_6$ DPs. The average crystallite size (D), dislocation density (δ), and micro-strain (ε) estimated from W-H analysis and Scherrer analysis

View Article Online
DOI: 10.1039/D5CP02259B

for all the samples are summarized in the supporting information (Table S1). The structural parameters for the (220) plane are also calculated and summarized in Table 1.

Table 1. Calculated structural parameters for the (220) plane from XRD.

Material	Angle of diffraction, 2θ (degree)	D (nm)	δ (x10^{14}) Lines/m^2	ε (x 10^{-3})	d, Å	a, Å
$Cs_2AgBiCl_6$	23.22	37.88	6.97	4.54	3.83	10.84
$Cs_2AgIn_{0.25}Bi_{0.75}Cl_6$	23.3	30.44	10.79	5.63	3.81	10.787
$Cs_2AgIn_{0.5}Bi_{0.5}Cl_6$	23.35	23.66	17.85	7.23	3.80	10.759
$Cs_2AgIn_{0.75}Bi_{0.25}Cl_6$	23.57	32.11	9.70	5.28	3.77	10.666
$Cs_2AgIn_{0.9}Bi_{0.1}Cl_6$	23.72	28.43	12.37	5.93	3.75	10.598
$Cs_2AgInCl_6$	23.87	23.23	18.54	21	3.72	10.530

3.1.2 Raman spectroscopy Analysis

The Raman spectra for $Cs_2AgIn_xBi_{1-x}Cl_6$ DPs are shown in Figure 1 (c). The 532 nm wavelength laser was used to obtain the spectra. From the series of $Cs_2AgIn_xBi_{(1-x)}Cl_6$ DPs, $Cs_2Ag\ In_xBi_{(1-x)}Cl_6$ (x = 0) DP consists of Cs^+ ions positioned in the core of cuboctahedron having alternate [$BiCl_6$] and [$AgCl_6$] octahedral units, resulting in the creation of a three-dimensional grid [51] whereas, the DP structure of $Cs_2AgIn_xBi_{(1-x)}Cl_6$ (x = 1) is obtained by alternating [$AgCl_6$] and [$InCl_6$] octahedra in all three directions forming a 3D framework.[52] The $Cs_2AgIn_xBi_{1-x}Cl_6$ DPs exhibit three vibrational modes. The band at approximately 114 cm^{-1} corresponds to the breathing vibration of Ag-Cl bonds with T_{2g} symmetry. Additionally, the peaks observed at approximately 220 cm^{-1} and 285 cm^{-1} correspond to the stretching vibrations of the $AgCl_6$ octahedron having E_g and A_{1g} symmetry, respectively. Upon increasing In content from 10 to 90%, we observed a shift in the peaks along with changes in the intensities of each peak. Group theory predicts three types of Raman modes for $Cs_2AgIn_xBi_{1-x}Cl_6$ (x=1): A_{1g}, E_g, and T_{2g}.[53] The peaks corresponding to these three modes occur at 113 (T_{2g}), 144 (E_g), and 300 (A_{1g}) cm^{-1}, respectively. The E_g and A_{1g} modes are assigned to the stretching vibrations of $AgCl_6$ and $InCl_6$ octahedra, respectively. There are two peaks corresponding to the T_{2g} mode with different frequencies, where the peak at a higher frequency is ascribed to the breathing of octahedra and the peak at a lower frequency is due to the translational

View Article Online
DOI: 10.1039/D5CP02259B

motion of the Cs^+ ion. [54] The slight shift in Raman peaks suggests that incorporating In into the host material has induced lattice strain, indicating an improvement in the crystallinity of the samples.

3.1.3 FE-SEM/EDS Analysis

Figure 1(d) is the field emission-scanning electron microscopy (FE-SEM) image for $Cs_2AgIn_xBi_{1-x}Cl_6$ (x = 0) DP captured at a 1 μm scale. The image shows the formation of cubic crystals. The FE-SEM images of $Cs_2AgIn_xBi_{1-x}Cl_6$ (x = 0.50, 0.75, 0.90, and 1.0) captured at a 200 nm scale are provided in Figure S4 of the supporting information. From FE-SEM images, it can be observed that the cubic crystal structure is maintained after In alloying. Compositional analysis of the $Cs_2AgIn_xBi_{1-x}Cl_6$ DPs is conducted using EDS. The EDS spectra for all samples are shown in Figure S5 of the Supporting Information. Elemental analysis using the EDS technique is employed to determine the actual concentration of Indium in the $Cs_2AgIn_xBi_{1-x}Cl_6$ NCs. The atomic percentage is listed in Table S3 of the supporting information. EDS spectra were acquired in the binding energy range of 0-15 keV for the $Cs_2AgIn_xBi_{1-x}Cl_6$ DPs, revealing a nearly stoichiometric composition of the synthesized material. Moreover, the atomic composition obtained closely corresponds to that of the metal salts used. The atomic composition analysis reveals a continuous decrease in the Bi content and an increase in the In content, with the latter rising during the synthesis. Elemental mapping images for $Cs_2AgIn_xBi_{1-x}Cl_6$ (x = 0, 0.50, 0.75, 0.9, 1.0) samples are shown in Figures S6 to S10, respectively, in the supporting information. EDS mapping images confirm the homogeneous dispersion of all elements within the synthesized materials.

3.1.4 Transmission Electron Microscopy (TEM) Analysis

The wide TEM images of $Cs_2AgIn_xBi_{1-x}Cl_6$ (x = 0, 1) and the corresponding histograms are shown in Figure S2 of the Supporting Information. The average particle size estimated for $Cs_2AgIn_xBi_{1-x}Cl_6$ (x = 0) DPs is around 24.7 nm, and it is 17.7 nm for $Cs_2AgIn_xBi_{1-x}Cl_6$ (x = 1). Figure 1(e) depicts the HR-TEM image of $Cs_2AgIn_xBi_{1-x}Cl_6$ (x = 1) NCs recorded at a resolution of 5 nm. The TEM image exhibits the cubic morphology of the $Cs_2AgIn_xBi_{1-x}Cl_6$ (x = 1) DP. As observed, the high-resolution TEM image (Figure 1(e)) reveals clear lattice fringes. For $Cs_2AgIn_xBi_{1-x}Cl_6$ (x =

View Article Online
DOI: 10.1039/D5CP02259B

1), the value of interplanar spacing is approximately 0.37 nm as derived from the TEM images, which represents the orientation along (220) planes. The selected-area electron diffraction (SAED) pattern of $Cs_2AgIn_xBi_{1-x}Cl_6$ (x = 1) shows concentric rings corresponding to the (220), (222), (400), (422), and (440) lattice planes as shown in Figure 1(f). These results are consistent with those obtained from XRD. The presence of prominent diffraction spots in the SAED pattern confirms the polycrystalline nature of the materials. Additional HR-TEM images at a resolution of 5 nm and the corresponding SAED patterns, along with the respective lattice planes for $Cs_2AgIn_xBi_{1-x}Cl_6$ DPs, are provided in Supporting Information (Figure S3).

Further, we have performed first-principles DFT calculations to characterize the structural and electronic structures of $Cs_2AgIn_xBi_{1-x}Cl_6$ (x = 0, 1). Both materials were modeled in the cubic $Fm\bar{3}m$ space group as displayed in Figure 1 (g and j). The optimized lattice parameter is calculated to be a=10.88 Å (1287.19 $Å^3$) for $Cs_2AgIn_xBi_{1-x}Cl_6$ (x = 0) and 10.61 Å (1194.59 $Å^3$) for $Cs_2AgIn_xBi_{1-x}Cl_6$ (x = 1), aligning well with the experimental findings. The observed contraction in the lattice parameter of $Cs_2AgIn_xBi_{1-x}Cl_6$ (x = 1) compared to $Cs_2AgIn_xBi_{1-x}Cl_6$ (x = 0) is consistent with the larger ionic size of Bi^{3+} (117 pm) than In^{3+} (94 pm). The partial density of states (PDOS) analysis demonstrated that the valence band (VB) edge of the $Cs_2AgIn_xBi_{1-x}Cl_6$ (x = 0) NCs (Figure 1(h)) is dominated by Cl-*p* and Ag-*d* orbitals, whereas the Bi-p orbitals dominate the conduction band (CB) edge.

View Article Online
DOI: 10.1039/D5CP02259B

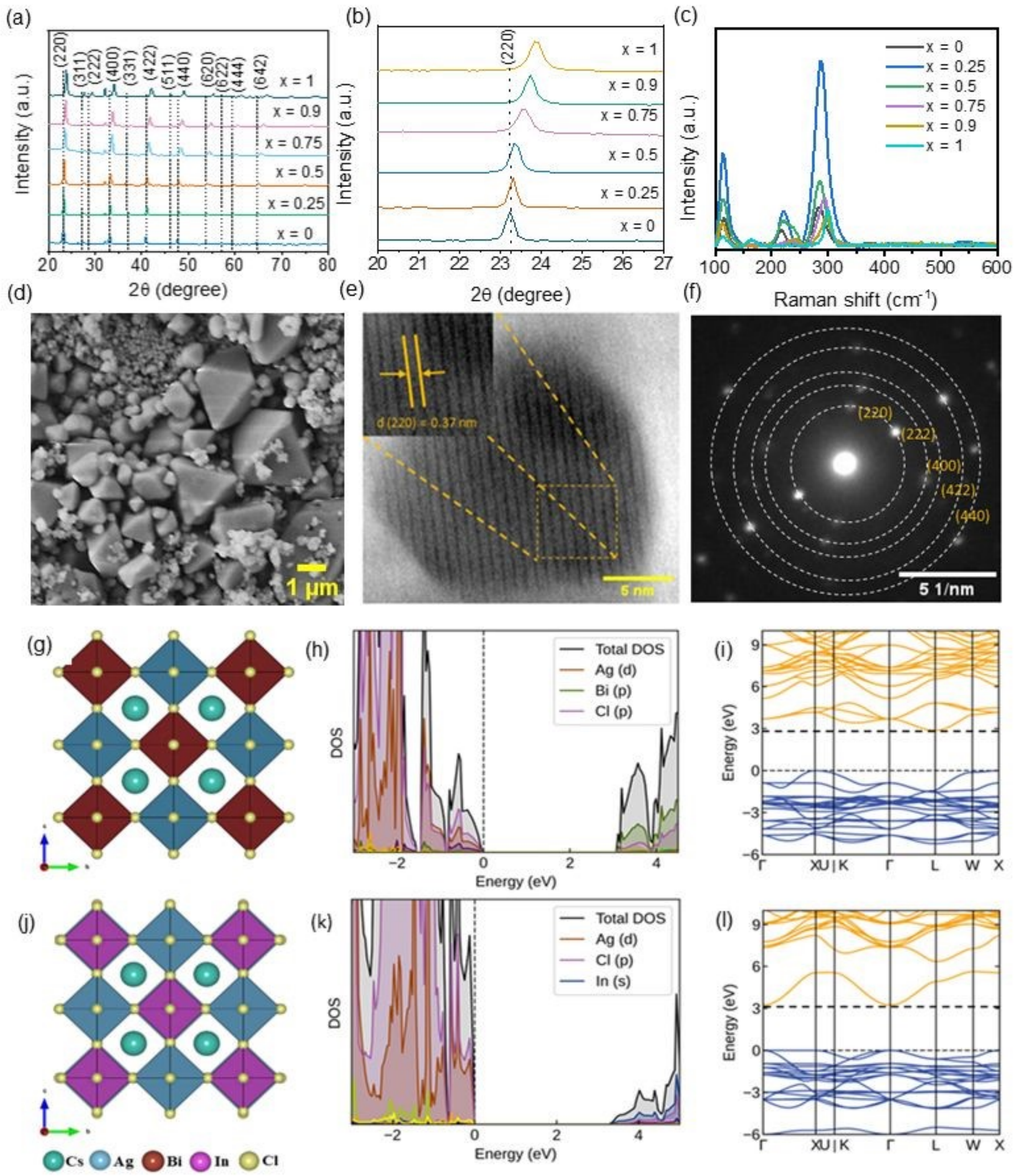

Figure 1. (a) XRD pattern of $Cs_2AgIn_xBi_{1-x}Cl_6$, (b) Zoomed XRD showing a clear shift towards higher angle. (c) Raman spectra of $Cs_2AgIn_xBi_{1-x}Cl_6$. (d) FE-SEM image of $Cs_2AgIn_xBi_{1-x}Cl_6$ (x = 0) sample. (e) and (f) are high-resolution TEM and SAED patterns for the $Cs_2AgIn_xBi_{1-x}Cl_6$ (x = 1) sample. (g) Crystal structure of $Cs_2AgIn_xBi_{1-x}Cl_6$ (x = 0). (h) The corresponding PDOS for $Cs_2AgIn_xBi_{1-x}Cl_6$ (x = 0). (i) Band structure of $Cs_2AgIn_xBi_{1-x}Cl_6$ (x = 0) along the high-symmetry directions of the Brillouin zone. (j) Crystal structure of $Cs_2AgIn_xBi_{1-x}Cl_6$ (x = 1) (k) The corresponding PDOS for $Cs_2AgIn_xBi_{1-x}Cl_6$ (x = 1). (l) Band structure of $Cs_2AgIn_xBi_{1-x}Cl_6$ (x = 1) along the high-symmetry directions of the Brillouin zone.

View Article Online
DOI: 10.1039/D5CP02259B

Similarly, for the $Cs_2AgIn_xBi_{1-x}Cl_6$ (x=1) NCs (Figure 1 (k)), the VB edge is dominated by Cl-*p* and Ag-*d* orbitals, whereas In-s dominates the CB edge. It is evident from the predicted electronic band structures displayed in Figure 1 (i) and (l) that the $Cs_2AgIn_xBi_{1-x}Cl_6$ (x=0) NCs exhibit an indirect band gap of 2.87 eV, whereas the $Cs_2AgIn_xBi_{1-x}Cl_6$ (x=1) NCs exhibit a direct band gap of 3.24 eV at the Γ-point on the Brillouin zone. These results confirmed the transition from indirect to direct with the complete replacement of Bi^{3+} with In^{3+} ions.

The effective masses values of electrons (m_e^*) and holes (m_h^*) along the directions of different Brillouin-zones in the $Cs_2AgIn_xBi_{1-x}Cl_6$ (x= 0.0, 1.0) NCs are determined using the Equation: $m_{e(h)}^* = \pm\, \hbar^2 \left(\frac{d^2E_k}{dk^2}\right)^{-1}$, where E_k is the energy of the band (i.e., CBM and VBM) as a function of the wave vector k, and $\hbar$ is the reduced Planck's constant. For $Cs_2AgIn_xBi_{1-x}Cl_6$ (x=0), the m_e^* (m_h^*) are calculated at 0.490 (−0.233 m_e) and 0.351 (−1.004 m_e) along the X–Γ and X–W directions, respectively. For $Cs_2AgIn_xBi_{1-x}Cl_6$ (x=1.0), the m_e^* (m_h^*) are predicted at 0.309 (−0.322 m_e), 0.316 (−0.450 m_e), and 0.319 (−0.666 m_e) along the Γ–X, Γ–K, and Γ–L directions, respectively. Generally, the predicted electron effective masses are smaller as compared to the hole effective masses, except for the X-Γ direction for $Cs_2AgBiCl_6$, suggesting a higher mobility for electrons than holes in these materials. The larger electron effective mass along the X-Γ direction for $Cs_2AgBiCl_6$ than that of the hole can be attributed to the small curvature (less dispersed bands) at the conduction band edge along the X-Γ direction compared to that of the valence band edge. The Bohr exciton radius is estimated for $Cs_2AgIn_xBi_{1-x}Cl_6$ (x = 0, 1) by using the results obtained from first principles DFT calculations. A detailed explanation can be found in the Supporting Information. The estimated Bohr radius is 1.3 nm for $Cs_2AgIn_xBi_{(1-x)}Cl_6$ (x = 0) and 0.82 nm for $Cs_2AgIn_xBi_{(1-x)}Cl_6$ (x = 1). These values are much smaller than the size of the crystals determined from the TEM histogram, strongly suggesting a weak quantum confinement in both materials.

3.1.5 X-ray Photoelectron Spectroscopy (XPS) Analysis

View Article Online
DOI: 10.1039/D5CP02259B

Figure 2 shows the XPS spectra of $Cs_2AgIn_xBi_{1-x}Cl_6$ NCs, revealing the presence of Cs, Ag, In, Bi, and Cl in the prepared NCs. To further comprehend the effect of incorporating In on the electronic properties, core level XPS spectra were recorded for Cs 3d, In 3d, Ag 3d, Cl 2p, and Bi 4f, and are displayed in Figure 2. The binding energy values for electrons were calculated, with correction for the shift in carbon 1s binding energy. For $Cs_2AgIn_xBi_{1-x}Cl_6$ ($x = 0$), Cs-$3d_{3/2}$ and Cs-$3d_{5/2}$ peaks are observed at 740.70 eV and 726.76 eV, as shown in Figure 2(a1).

View Article Online
DOI: 10.1039/D5CP02259B

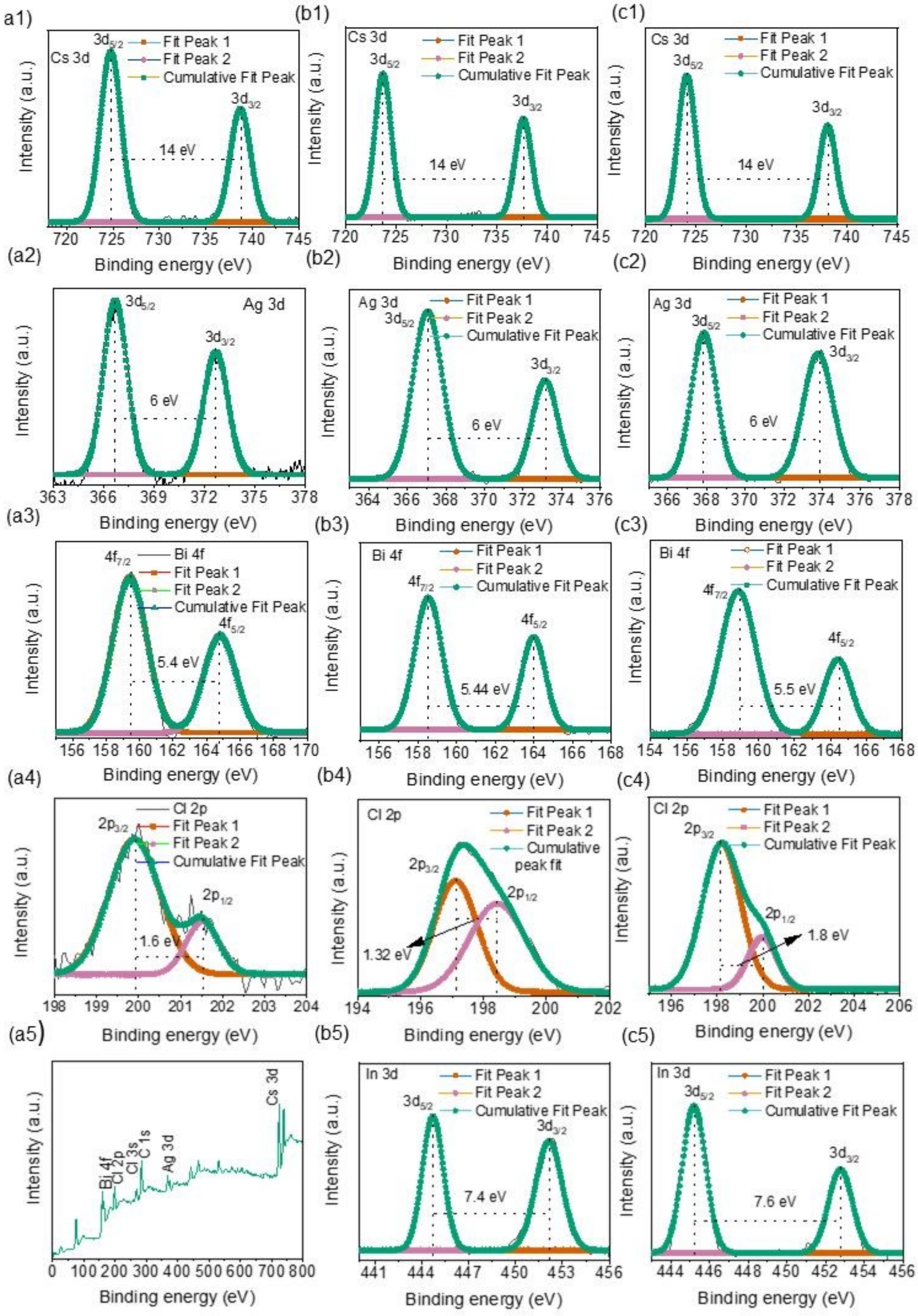

Figure 2. (a1-a5) Narrow scan and survey scan XPS for $Cs_2AgIn_xBi_{1-x}Cl_6$ (x = 0) sample. (b1-b5) are the narrow scan XPS spectra of the $Cs_2AgIn_xBi_{1-x}Cl_6$ (x = 0.5) sample. (c1-c5) are the narrow scan XPS spectra of the $Cs_2AgIn_xBi_{1-x}Cl_6$ (x = 0.75) sample.

View Article Online
DOI: 10.1039/D5CP02259B

In the narrow Ag 3d XPS spectrum, peaks around 376 eV and 370 eV (Figure 2, a2) correspond to Ag-3d$_{3/2}$ and Ag-3d$_{5/2}$. The Bi-4f spectrum exhibits a doublet at 161.43 eV and 166.80 eV, indicating Bismuth in a 3+ state. Cl 2p spectra display peaks at approx. 202 eV and 204 eV for Cl 2p$_{3/2}$ and Cl 2p$_{1/2}$. For the $Cs_2AgIn_xBi_{1-x}Cl_6$ (x = 0.5) sample, the two peaks are detected in the elemental scan of Cs 3d located at 723.70 eV and 737.66 eV.

These peaks are associated with the Cs 3d$_{5/2}$ and Cs 3d$_{3/2}$ states. The narrow scan XPS of Ag reveals peaks at around 367 eV and 373 eV for 3d$_{5/2}$ and 3d$_{3/2}$ respectively. The two peaks at 158.55 eV and 164 eV in the narrow scan XPS of Bi 4f signify Bi 4f$_{7/2}$ and 4f$_{5/2}$ states. The narrow scan of In 3d exhibits peaks at 444.73 eV and 452.14 eV. Cl 2p narrow scan deconvolution reveals levels at 197.11 eV and 198.44 eV for 2p$_{3/2}$ and 2p$_{1/2}$ (Figure 2(b1-b5)). For $Cs_2AgIn_xBi_{1-x}Cl_6$ (x = 0.75) (Figures 2(c1-c5)), narrow scan XPS of Cs 3d shows peaks at 738 eV (3d$_{3/2}$) and 724 eV (3d$_{5/2}$).

Ag elemental scan reveals peaks around 367.8 eV and 373.8 eV for Ag 3d$_{5/2}$ and Ag 3d$_{3/2}$, respectively. Bi 4f narrow scan displays a doublet at 158.88 and 164.42 eV for Bi 4f$_{7/2}$ and 4f$_{5/2}$, respectively. In 3d narrow scan exhibits peaks at 445.18 eV and 452.6 eV for In 3d$_{5/2}$ and 3d$_{3/2}$ states, respectively. Cl 2p narrow scan deconvolution reveals levels at 198.19 eV and 199.98 eV for 2p$_{3/2}$ and 2p$_{1/2}$. No extra peak was observed in any of the narrow scans, indicating that there is no metallic phase present for any of the elements. The narrow scan XPS spectrum of Cesium in $Cs_2AgIn_xBi_{1-x}Cl_6$ (x = 1) shows two spin-orbit states at 723.58 eV and 737.45 eV for 3d$_{5/2}$ and 3d$_{3/2}$, respectively (Figure S12, b2-b5 of supporting information). [31] The peaks observed at 367.22 eV and 373.25 eV are attributed to the Ag 3d$_{5/2}$ and 3d$_{3/2}$ levels, respectively, which confirms that Ag is present in the +1 oxidation state. In the narrow scan XPS spectrum, two peaks corresponding to the In 3d$_{5/2}$ and 3d$_{3/2}$ states are observed at 444.44 eV and 452 eV, respectively. [55] The deconvolution of the narrow scan XPS spectrum of chlorine shows 2p$_{3/2}$ and 2p$_{1/2}$ fine levels at 197.66 and 199.29 eV, respectively. The XPS spectra of $Cs_2AgIn_xBi_{1-x}Cl_6$ (x = 0.1, 0.25, 0.90, 1.0) are provided in supporting information Figures S11 and S12.

3.2. Optical properties of $Cs_2AgIn_xBi_{(1-x)}Cl_6$ DPs

3.2.1. UV-Visible Spectroscopy

View Article Online
DOI: 10.1039/D5CP02259B

Figure 3(a) displays the optical absorption spectra of $Cs_2AgIn_xBi_{(1\text{-}x)}Cl_6$ derived from diffuse reflectance spectra. An excitonic peak at 365 nm and a tail extending towards higher wavelengths is observed in the UV-vis spectrum. spectrum of $Cs_2AgBiCl_6$ (x = 0). The origin of this peak is from Bismuth $6s^2$-$6s^1$ $6p^1$ direct transition, whereas the long tail arises due to the transitions related to the trap state along with the indirect band gap. [25,28,30] An indirect band gap transition is an inherent property of a material that results in a low photoluminescence quantum efficiency (PLQE). These findings suggest that the $Cs_2AgIn_xBi_{1\text{-}x}Cl_6$ (x = 0) NCs are not appropriate for application in the field of optoelectronics. [56] As the In content is increased, the absorption peak shows a blue shift, and the absorption tail is reduced. The absorption edge is relatively sharp for the In contents of 75% and 90%, highlighting the direct band gap of $Cs_2AgIn_xBi_{(1-x)}Cl_6$ (x = 0.75 and 0.9). The absorption peak is located at ~280 nm in the case of $Cs_2AgIn_xBi_{1\text{-}x}Cl_6$ (x = 1), with a band gap value of 3.5 eV. This DP exhibits poor absorption near the band gap; therefore, it is not a suitable choice for optoelectronic applications. [57] The values of the band gap were estimated by using the following equation:

$$[F(R_\infty)h\nu]^n = A\,(h\nu - E_g) \tag{5}$$

where, hν represents incident energy, A is the proportionality constant, E_g represents the optical band gap. *n* is an integer, and its values are 2 and ½ for the allowed direct and indirect transitions, respectively. $F(R_\infty)$ is the Kubelka-Munk function, which is expressed as,

$$F(R_\infty) = \frac{(1-R)^2}{2R} = \frac{K}{S} \tag{6}$$

where R, K, and S are the reflection, absorption, and scattering coefficients, respectively.

For $Cs_2AgIn_xBi_{1\text{-}x}Cl_6$ (x = 0, 0.25, 0.5) samples, the band gap is determined by extrapolation of the linear portion of $[F(R_\infty)\ (h\nu)]^{1/2}$ versus hν in the Tauc plot (Figure S13). The band gap value increases from 2.71 eV for the pristine sample (x = 0) to 2.81 eV for the $Cs_2AgIn_xBi_{1\text{-}x}Cl_6$ (x = 0.5) sample. The band gap variation can be attributed to changes in the electronic structure of the

View Article Online
DOI: 10.1039/D5CP02259B

material. On the other hand, as it is well reported that above 50% In content, the band gap nature changes from indirect to direct, the band gap values for the samples with In content more than 50% are determined by extrapolation of the linear region in $[F(R_\infty)h\nu]^2$ versus hν (Figure S12). [33] The estimated optical band gap values are provided in Table S2 of the Supporting Information. The optical properties of $Cs_2AgIn_xBi_{1-x}Cl_6$ (x = 0, 1) DPs (Figure 3 (b-e)) show that they exhibit weak optical absorption around the band gap. $Cs_2AgIn_xBi_{1-x}Cl_6$ (x = 0) has a higher dielectric constant (3.89) than $Cs_2AgIn_xBi_{1-x}Cl_6$ (x = 1) (2.89), indicating its higher ability to screen charge carriers and reduce recombination rates. The $Cs_2AgIn_xBi_{1-x}Cl_6$ (x = 0) material also possesses higher reflectivity and refractive index than $Cs_2AgIn_xBi_{1-x}Cl_6$ (x = 1), as shown in Figure 3 (d and e).

3.2.2. Photoluminescence (PL) studies

The In-alloyed DP NCs were further characterized through room-temperature photoluminescence (PL). Figure 3(f) is the Jacobian transformed PL spectra of $Cs_2AgIn_xBi_{(1-x)}Cl_6$ NCs. All samples were excited using a wavelength of 365 nm. The room temperature PL of $Cs_2AgIn_xBi_{1-x}Cl_6$ (x=0) exhibits broadband emission, featuring an excitonic peak around 575 nm alongside emissions related to defects. For $Cs_2AgIn_xBi_{1-x}Cl_6$ (x = 0.0, 0.25, and 0.50), the PL profiles closely resemble that of the $Cs_2AgIn_xBi_{1-x}Cl_6$ (x = 0) sample, differing primarily in the intensity. Nonetheless, peak positions exhibit slight shifts, suggesting tunability in the emission wavelengths of the NCs consistent with the absorption spectroscopy results. As the In content increases above 50%, dual emissions emerge in the PL spectra, observed in the blue-violet and orange regions. Out of them, the narrow peak located at high energy in PL of $Cs_2AgIn_xBi_{1-x}Cl_6$ (x = 0.75, 0.90) likely originates from the free exciton emission, whereas the broad low energy peak is ascribed to the emissions coming from defects or self-trapped excitons (STEs). In contrast to free excitons, defects and STEs emission spectra are broad with a large Stoke's shift from the absorption. Initially, the PL peak gradually rises, but beyond x = 0.75, the intensity experiences a sudden increase. The photoluminescence excitation spectra for all the samples were recorded and are depicted in Figure S18 of the supporting information. Figure S18 (a), (b), and (c) reveal that the PLE spectrum has its onset wavelength lower than the absorption onset, further confirming the indirect band gap nature of $Cs_2AgIn_xBi_{1-x}Cl_6$ (x = 0, 0.25, 0.5). Figure S18 (d-g) represents the PLE spectra recorded for $Cs_2AgIn_xBi_{1-x}Cl_6$ (x = 0.75, 0.90) samples corresponding to emissions in violet/blue as well as

View Article Online
DOI: 10.1039/D5CP02259B

the yellow/orange region. The excitation spectra for $Cs_2AgIn_xBi_{1-x}Cl_6$ (x = 0.75, 0.90) samples corresponding to emissions in the blue-violet region ideally overlap with the absorption spectra of these samples, confirming that the materials can be assigned as a direct band gap material. Furthermore, it is confirmed that the broad orange/yellow emissions in the case of

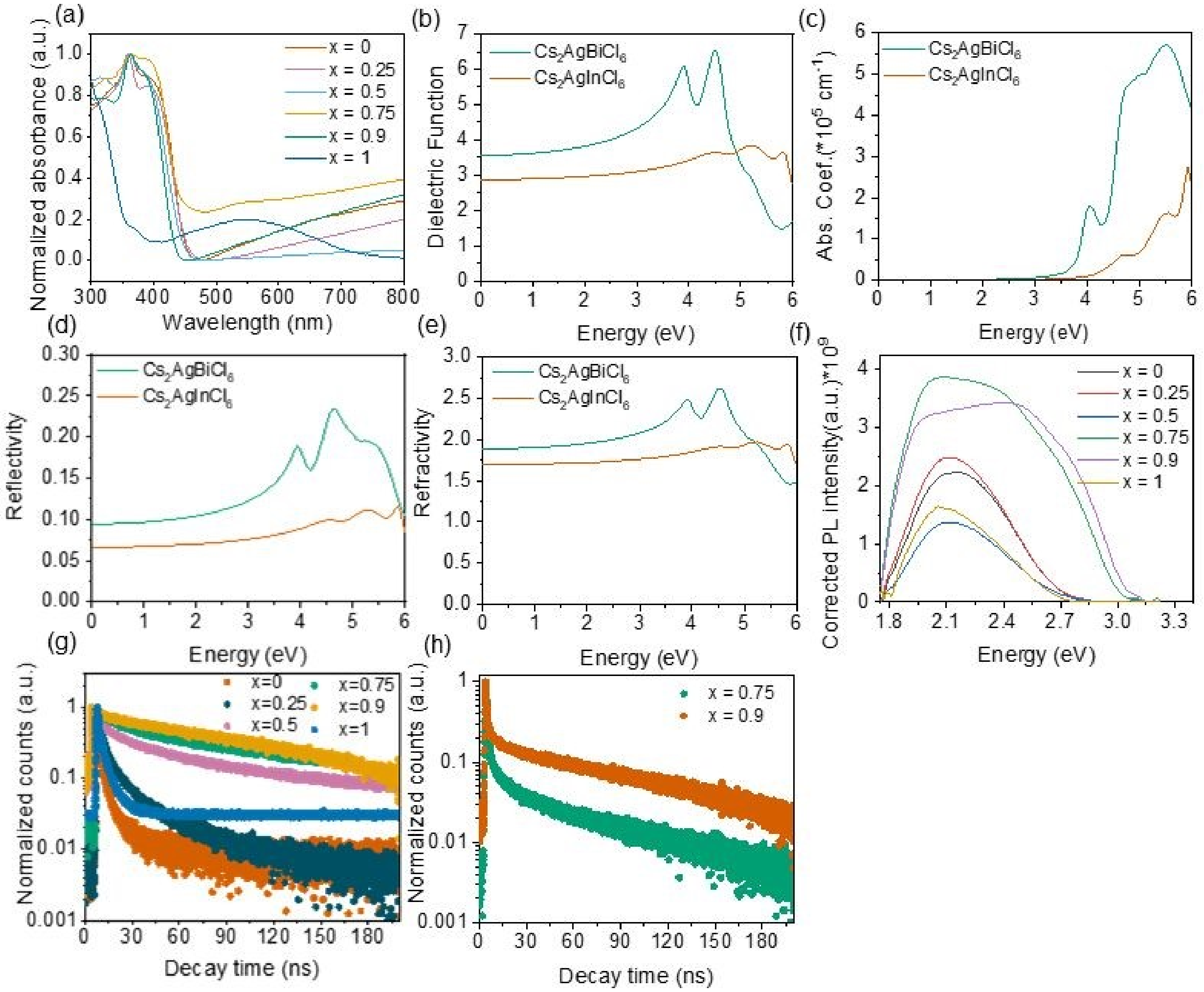

Figure 3. (a) Optical absorption spectra of $Cs_2AgIn_xBi_{(1-x)}Cl_6$ derived from diffuse reflectance spectra, (b-e) DFT calculated optical properties of $Cs_2AgIn_xBi_{1-x}Cl_6$ (x = 0) and $Cs_2AgIn_xBi_{1-x}Cl_6$ (x = 1): (b) dielectric function, (c) absorption coefficient, (d) reflectivity, and (e) refractive index. (f) Jacobian transformed room temperature PL spectra of $Cs_2AgIn_xBi_{(1-x)}Cl_6$ (g and h) TRPL traces of $Cs_2AgIn_xBi_{(1-x)}Cl_6$ corresponding to emissions towards higher wavelength and lower wavelength, respectively.

View Article Online
DOI: 10.1039/D5CP02259B

$Cs_2AgIn_xBi_{1-x}Cl_6$ (x = 0.75, 0.90) samples are attributed to the excited state defects, indicating that there is a slight change in the crystal structure of the material.

3.2.3. Time-Resolved Photoluminescence (TRPL) Analysis

To confirm the origin of dual emission in the synthesized $Cs_2AgIn_xBi_{(1-x)}Cl_6$ DP NCs, TRPL measurements were carried out. A picosecond 405 nm laser diode is used as an excitation source, which can generate a pulse width shorter than 70 ps. The decay curves for all the samples were recorded corresponding to the broad emission, and the decay traces are shown in Figure 3(g). The decay traces for $Cs_2AgIn_xBi_{1-x}Cl_6$ (x = 0.75, 0.9) samples, which correspond to the violet/blue emissions, is shown in Figure 3(h). The emission decay traces are fitted with a function:

$$A(t) = A_1 \exp\left(\frac{-t}{\tau_1}\right) + A_2 \exp\left(\frac{-t}{\tau_2}\right) \quad (7)$$

where τ_1 and τ_2 are the decay components. The first-short lifetime PL component in bi-exponential decay is from excitonic recombination, while the second-long lifetime PL component is due to the trap state-related excitonic recombination. The average lifetime (t) is calculated using the formula:

$$t_{av} = \frac{A_1 {\tau_1}^2 + A_2 {\tau_2}^2}{A_1 \tau_1 + A_2 \tau_2} \quad (8)$$

For $Cs_2AgIn_xBi_{1-x}Cl_6$ (x = 0.75, or x = 0.9) samples, the decay traces corresponding to violet/blue emission show quick decay, while the decay corresponding to orange/yellow PL is much slower (Table S4). The distinctly different decay profiles of the two emissions indicated that their origins are different. For $Cs_2AgIn_xBi_{1-x}Cl_6$ (x = 0.75, 0.9) samples, the TRPL corresponding to a high energy peak shows fast decay of less than 2 ns. The lifetime values calculated for broad orange/yellow emissions are approximately 141 ns and 167 ns, respectively, for $Cs_2AgIn_xBi_{1-x}Cl_6$ (x = 0.75, 0.9) samples. The TRPL calculations showed a sudden increase in the lifetime of charge carriers on increasing the concentration of In up to 90%, and it again decreased suddenly at x = 1, indicating the excellent optical properties of $Cs_2AgIn_xBi_{1-x}Cl_6$ (x = 0.75, 0.9). The lifetime values

View Article Online
DOI: 10.1039/D5CP02259B

calculated from TRPL measurements and the contributions from short and long decay components are listed in Table 2.

Table 2. Calculated decay components (τ_1 and τ_2) and average carrier lifetime (t) for $Cs_2AgIn_xBi_{(1-x)}Cl_6$.

Material	$\tau_{1,}$ ns	%A_1	$\tau_{2,}$ ns	%A_2	t, ns	R^2
$Cs_2AgBiCl_6$	1.09	99.92	5.92	0.08	1.11	0.997
$Cs_2AgIn_{0.25}Bi_{0.75}Cl_6$	2.67	97.09	17.60	2.91	5.13	0.996
$Cs_2AgIn_{0.5}Bi_{0.5}Cl_6$	5.45	67.54	48.07	32.46	39.94	0.997
$Cs_2AgIn_{0.75}Bi_{0.25}Cl_6$	15.35	59.51	158.79	40.49	140.95	0.96
$Cs_2AgIn_{0.9}Bi_{0.1}Cl_6$	9.85	25.98	170.16	74.02	166.97	0.992
$Cs_2AgInCl_6$	1.56	98.43	5.76	1.57	1.79	0.999

3.3. Electrochemical measurements

Figure 4 (a) shows the cyclic voltammogram of $Cs_2AgIn_xBi_{(1-x)}Cl_6$ (x = 0) DP recorded at a 50 mV scan rate. The CV measurements were performed to examine the electronic band structure of the synthesized $Cs_2AgIn_xBi_{(1-x)}Cl_6$ DP materials. The blank CV was recorded in the DCM-TBAP mixture to verify the absence of any redox processes. The working electrode was fabricated by drop-casting 50 μL (at a concentration of 1 mg/mL) of the perovskite sample and subsequently drying under vacuum. The cyclic voltammograms for the $Cs_2AgIn_xBi_{(1-x)}Cl_6$ (x = 0.25, 0.5, 0.75, 1) DPs are shown in Figure 4 (b-e), respectively. The CV recorded for $Cs_2AgIn_xBi_{(1-x)}Cl_6$ (x = 0) sample shows two distinct peaks corresponding to the oxidation and reduction taking place at the respective electrodes. The peak at 1.98 V is the anodic (oxidation) peak that corresponds to the removal of an electron from the VB. On the other hand, the peak at -0.7 V is the cathodic (reduction) peak that corresponds to the addition of an electron to the CB. The CB edge and VB edge positions with respect to the vacuum level for the x = 0 sample are -3.8 and -6.48 eV, respectively. The electrochemical band gap (E_c) is determined as a potential difference between the anodic and cathodic peaks observed from the redox reactions taking place at the

View Article Online
DOI: 10.1039/D5CP02259B

semiconductor-electrolyte interface, and it is measured at 2.68 eV for the $Cs_2AgIn_xBi_{1-x}Cl_6$ (x = 0) sample. This is consistent with the optical band gap value determined from UV-vis. spectroscopy. The comparison of the optical and electrochemical band gap values is shown in Figure S15 of the supporting information. The same procedure was followed to determine the band gap and positions of band edges for other materials. The observed anodic and cathodic peak positions obtained are shown in Table 3. The band edge positions for all the samples are determined with respect to the normal hydrogen electrode (NHE) and local vacuum and summarized in Table 3 below. [42,58] Scan rate-dependent CV measurements were performed for the $Cs_2AgIn_xBi_{1-x}Cl_6$ (x = 0.25) sample to investigate the scan rate dependence of current. The CV recorded with increasing scan rates is shown in Figure 4 (f and g). The linearly increasing current with the square root of scan rate for cathodic and anodic peaks suggests that the reaction is diffusion-controlled. [39, 58,59] Figure 4 (h) displays the band alignment diagram of $Cs_2AgIn_xBi_{(1-x)}Cl_6$ (x = 0.0, 0.25, 0.50, 0.75, 1.0). The figure shows the CBM and VBM positions determined for these materials' vs local vacuum, as well as the electrochemical band gaps estimated from the CV measurements.

View Article Online
DOI: 10.1039/D5CP02259B

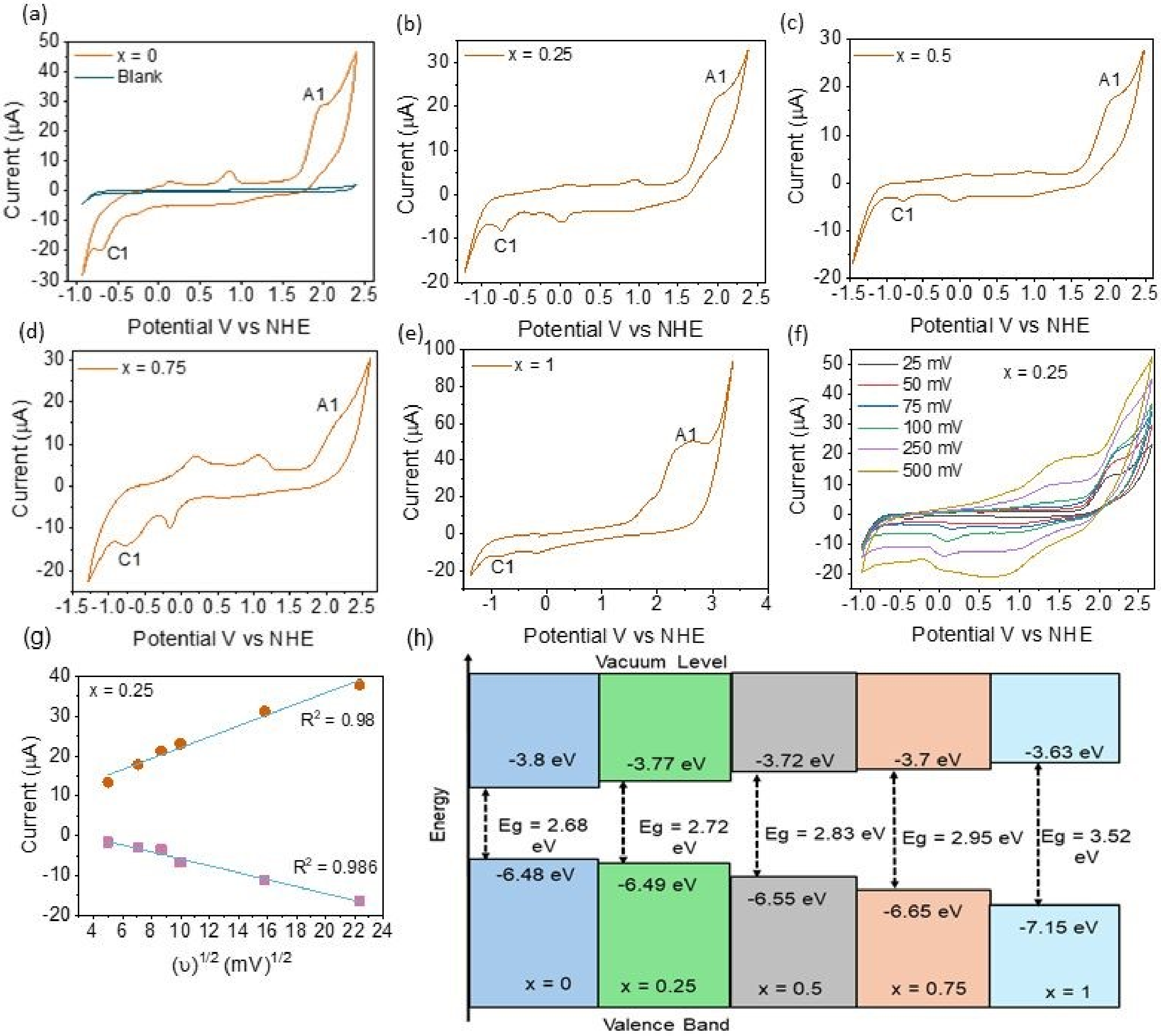

Figure 4: (a) Cyclic Voltammogram of $Cs_2AgIn_xBi_{1-x}Cl_6$ (x = 0) sample compared with blank CV. (b-e) Cyclic Voltammograms of $Cs_2AgIn_xBi_{1-x}Cl_6$ (x = 0.25, 0.5, 0.75 and 1 respectively) (f) Scan rate dependent CV for $Cs_2AgInxBi_{(1-x)}Cl_6$; x = 0.25 sample (g) Linear fitting of the scan rate dependent CV data as square root of scan rate vs current using Randles-Sevcik equation for $Cs_2AgIn_xBi_{(1-x)}Cl_6$; x = 0.25 sample (h) Band alignment diagram.

Table 3: The VB and CB edge positions vs NHE and vacuum, and electrochemical band gap evaluated using CV measurements.

View Article Online
DOI: 10.1039/D5CP02259B

Sample	CBM vs NHE (V)	VBM vs NHE (V)	CBM vs Vacuum (eV)	VBM vs Vacuum (eV)	E_c (eV)	E_g (eV)
$Cs_2AgBiCl_6$	-0.7	1.98	-3.8	-6.48	2.68	2.70
$Cs_2AgIn_{0.25}Bi_{0.75}Cl_6$	-0.73	1.99	-3.77	-6.49	2.72	2.71
$Cs_2AgIn_{0.5}Bi_{0.5}Cl_6$	-0.78	2.05	-3.72	-6.55	2.83	2.81
$Cs_2AgIn_{0.75}Bi_{0.25}Cl_6$	-0.8	2.15	-3.7	-6.65	2.95	2.89
$Cs_2AgInCl_6$	-0.87	2.65	-3.63	-7.15	3.52	3.53

3.4. Temperature Dependent PL

Figure 5 displays the Jacobian transformed PL spectra of $Cs_2AgIn_xBi_{(1-x)}Cl_6$ (x = 0, 0.75, 0.9) recorded from 80 K to 300 K. Excitation of the samples was achieved using a wavelength of 365 nm. The PL exhibits broadband emission, attributed to self-trapped excitons (STEs). The broad PL emission is elucidated by the self-trapped states induced by exciton-phonon coupling. To assess the exciton-phonon coupling strength, TDPL measurements were carried out. For $Cs_2AgIn_xBi_{(1-x)}Cl_6$ (x = 0) DPs, when the temperature rises from 80 K to 300 K, the intensity of the peak is reduced along with the broadening of peaks. Additionally, the peak is blue-shifted up to 200K, followed by a red shift with higher temperature. These shifts can be attributed to lattice distortion and changes in the valence band concerning temperature variations. The Jacobian transformed TDPL spectra for $Cs_2AgIn_xBi_{(1-x)}Cl_6$ (x = 0.25, 0.5, 1) are shown in Figure S16 of the supporting information. The intensity of PL peaks first increases up to 160 K, and it again decreases for higher temperatures in the case of $Cs_2AgIn_xBi_{(1-x)}Cl_6$, x = 0.25 and x = 0.5 samples. The FWHM broadens with an increase in temperature. Also, there is a blue shift in PL peak positions. In the case of $Cs_2AgIn_xBi_{(1-x)}Cl_6$ (x = 1) sample, the intensity decreases monotonically along with the blue shift in PL peaks. For $Cs_2AgIn_xBi_{(1-x)}Cl_6$ (x = 0.75, 0.90) samples, the emission originating from STEs became dominant over the free exciton emission with decreasing temperature from 300 K to 80 K, as shown in Figure 5 (b and c). The peak position of STE PL exhibited a slight red shift,

DOI: 10.1039/D5CP02259B

while that of the free exciton PL was unchanged when the temperature decreased. As can be seen clearly, the STEs' peak profile became comparatively narrower with a decrease in temperature. Non-radiative recombination is hindered at low temperatures, and hence, we get maximum intensity at lower temperatures.

The corrected PL intensity vs inverse temperature is (Figure 5) fitted with $R^2 \sim 1$ using an Arrhenius equation:

$$I(T) = \frac{I_0}{1+A\exp(\frac{-Ea}{k_bT})} \tag{9}$$

where I(T) and I_0 are the corrected PL intensity values at temperature T and zero K, respectively.

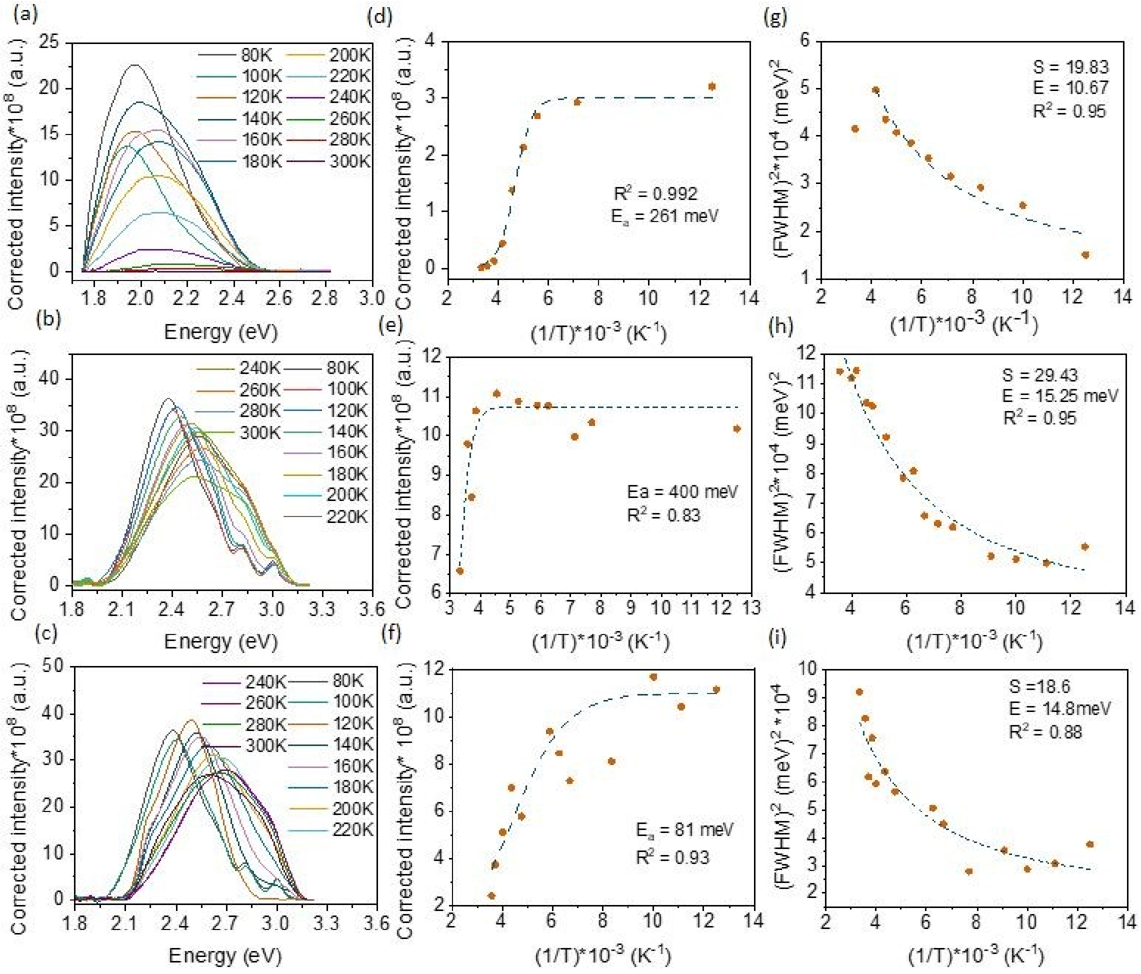

Figure 5. (a), (b), and (c) are the Jacobian transformed TDPL spectra of $Cs_2AgIn_xBi_{(1-x)}Cl_6$ recorded in the temperature range 80 K – 300 K. (x = 0, x = 0.75 and x = 0.9 respectively) (d), (e) and (f) are the corrected

View Article Online
DOI: 10.1039/D5CP02259B

intensity vs inverse temperature graphs fitted using an Arrhenius function for samples $Cs_2AgIn_xBi_{(1-x)}Cl_6$; x = 0, x = 0.75, and x = 0.90, respectively. (g), (h), and (i) are the $(FWHM)^2$ vs (1/T) graphs for $Cs_2AgIn_xBi_{(1-x)}Cl_6$; x = 0, x = 0.75, and x = 0.90, respectively.

A is a constant, k_b is the Boltzmann constant, and E_a is the activation energy. The activation energy values extracted are provided in Table S5 of the supporting information. The minimum activation energy for $Cs_2AgIn_xBi_{(1-x)}Cl_6$ (x = 0.9) sample indicates a significant reduction in non-radiative recombinations, thereby confirming the enhanced optical performance of the sample. The decreased intensity is associated with the peak broadening and is attributed to phonon-mediated self-trapped excitonic recombination. The change in intensity is attributed to the trapping and detrapping of excitons through thermally activated STE states. To study the effect of exciton-phonon coupling, the temperature dependence of peak broadening is examined with the help of the equation:

$$FWHM = 2.36\sqrt{S}\ \hbar\omega_{phonon}\sqrt{\coth\frac{\hbar\omega_{phonon}}{2k_bT}} \tag{10}$$

where $\hbar\omega_{phonon}$ is the phonon energy and S is the Huang-Rhys factor, which gives the strength of exciton-phonon coupling in the material. By fitting the temperature-dependent FWHM broadening, the values of the Huang-Rhys factor and optical phonon energy were determined. The calculated values of S and $\hbar\omega_{phonon,}$ along with the corresponding R^2 values, are shown in Table S5 of the supporting information. Here, $Cs_2AgIn_xBi_{(1-x)}Cl_6$ (x = 0.9) exhibits the lowest value of S, indicating a reduction in the strength of exciton-phonon coupling upon In incorporation. Moreover, the S value is moderate for all samples, as observed in Table S5, which can balance the exciton-phonon coupling in the material. The deconvoluted TDPL spectra for $Cs_2AgIn_xBi_{(1-x)}Cl_6$ (x = 0, 0.75, 0.9) are shown in Figure S17 of the supporting information. The details are provided in the supporting information.

Photodetector Measurements

Figure 6 displays the current-voltage (I-V) characteristics of $Cs_2AgIn_xBi_{(1-x)}Cl_6$ films under dark and white light illumination conditions. The I–V characteristics of films with a voltage sweep in

View Article Online
DOI: 10.1039/D5CP02259B

the range of -1.0 V to +1.0 V are shown in Figure 6 (a, d, g). The non-linear behavior of all I–V curves confirms the formation of a Schottky contact. The photoresponse of films is measured under alternating dark and white light illumination (30 mW/cm²) at zero bias voltage at room temperature. When light is incident on the device, the absorber material (perovskite layer) absorbs photons, generating electron-hole pairs (excitons). The electrons are selectively extracted by the TiO_2 layer and move towards the FTO, leaving behind the holes. The electrons then flow through the external circuit to the graphite electrode, where they recombine with the holes, completing the circuit and generating a photocurrent. To check the response of the devices, the light source is switched ON and OFF at 20 s intervals. The photo response measured for the three devices for 10 cycles is shown in Figure 6 (c, f, i). At zero bias, all the devices show current in μA range. Among the three materials, $Cs_2AgIn_xBi_{(1-x)}Cl_6$ (x = 0.9) exhibits the highest photocurrent and maintains excellent photocurrent stability over time, without a reduction in photocurrent. This implies that the device based on $Cs_2AgIn_xBi_{(1-x)}Cl_6$ (x=0.90) absorber material can show excellent photovoltaic performance with good stability.

View Article Online
DOI: 10.1039/D5CP02259B

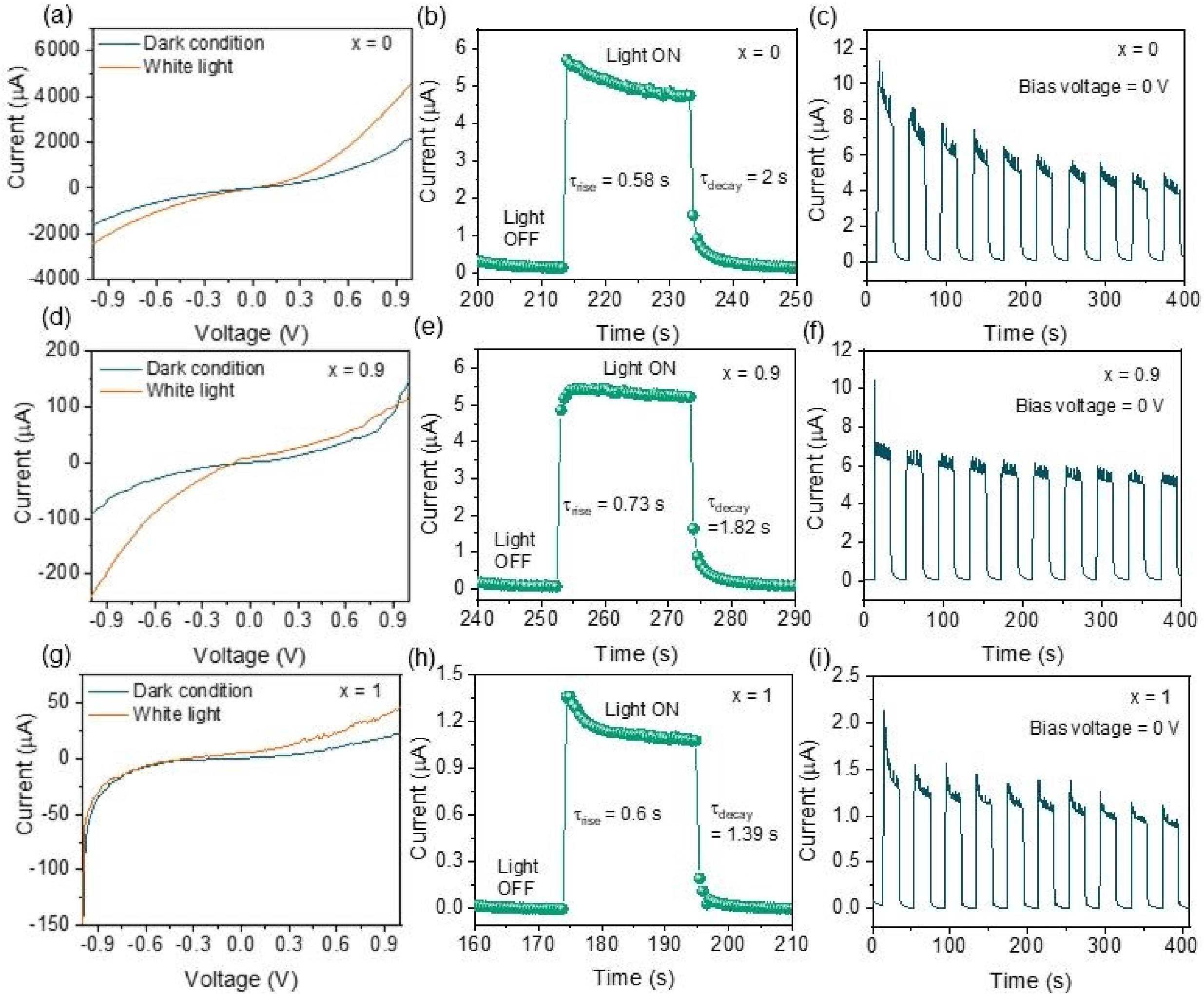

Figure 6: $Cs_2AgIn_xBi_{(1-x)}Cl_6$ double perovskite-based photodetector device characteristics. (a, d and g) I–V characteristics of $Cs_2AgIn_xBi_{(1-x)}Cl_6$ (x = 0, 0.9, 1) under white and dark light illumination (b, e and h) current versus time plot under dark and white light illumination for $Cs_2AgIn_xBi_{(1-x)}Cl_6$ (x = 0, 0.9, 1) (c, f and i) current versus time single-cycle plots of $Cs_2AgIn_xBi_{(1-x)}Cl_6$ (x = 0, 0.9, 1) respectively.

It shows a constant current over the cycles, indicating its good stability and repeatability. The high value of current may be attributed to its high absorption coefficient and reduced defect states, as evidenced by the optical properties. Also, the reduced trap states reduce recombination of charge carriers, increasing the photocurrent. The performance of photodetectors is characterized by various parameters, including photoresponsivity and detectivity. The photoexcited current generated per unit power of incident light on the effective area of a photodetector is called photoresponsivity [60] and is calculated by,

$$R_\lambda = \frac{\Delta I}{P_\lambda * A}, \tag{11}$$

View Article Online
DOI: 10.1039/D5CP02259B

where I = I_{photo} - I_{dark} is the change in photocurrent due to light incident on the effective photo-sensing area, P_λ is the intensity of incident light (30 mW/cm^2), and A is the active area of the film (1.5*1.5 cm^2). For photodetectors, detectivity (*D**) measures the quality of the detector. It is measured in Jones, and is expressed as: [61]

$$D^* = \frac{R_\lambda}{(2e*J_{dark})^{1/2}} \tag{12}$$

where J_{dark} is the dark current density and e is the electron charge. The values of photoresponsivity and detectivity extracted from the obtained data are provided in Table S6 of the supporting information. As evidenced by the results, the responsivity and detectivity values extracted are maximum for the $Cs_2AgIn_xBi_{(1-x)}Cl_6$ (x = 0.9) sample, indicating improved optoelectronic performance. The rise time (τ_{rise}) is defined as the time needed for a photodetector to change from 10% to 90% of its maximum photocurrent from its dark current value. Likewise, the decay time (τ_{decay}) is the time required for the photodetector to decrease from 90% to 10% of its minimum dark current value, starting from its photocurrent value. A single photo response cycle was analyzed, and the rise (τ_r) and decay times (τ_d) were estimated from it. The rise times and decay times calculated for all three samples are presented in Table S6 of the Supporting Information. Table S7 in the Supporting Information summarizes the reported device architectures and the key parameters of perovskite photodetectors. The table compares our results with representative values reported for lead halide perovskites and other DPs in recent literature.

4. Conclusions

In summary, we have successfully synthesized cubic-phase $Cs_2AgIn_xBi_{(1-x)}Cl_6$ materials by the antisolvent recrystallization method. EDS compositional analysis demonstrates successful incorporation and homogeneous distribution of In into the $Cs_2AgBiCl_6$ framework. Complementary first-principles DFT calculations confirm the transition from indirect band gap $Cs_2AgIn_xBi_{(1-x)}Cl_6$ (x=0) to the direct band gap $Cs_2AgIn_xBi_{(1-x)}Cl_6$ (x=1) at the Γ-point on the Brillouin zone. Absorption spectra indicate a long tail towards higher wavelengths, suggesting that the sub-bandgap state transition could arise from the trap states. PL measurements reveal a drastic

View Article Online
DOI: 10.1039/D5CP02259B

increase in intensity above 75% In concentration with dual emission, whereas the TRPL results show an increase in average lifetime values with an increase in In content, suggesting that the materials have excellent optical properties and are hence suitable candidates for optoelectronics. The TDPL results yield a moderate value of the Huang-Rhys factor, which can balance the exciton-phonon coupling, leading to high PLQY values. The optimized lattice parameters and band gap values calculated from DFT analysis closely match the experimental values. The photodetector measurements of $Cs_2AgIn_xBi_{(1-x)}Cl_6$ (x = 0.90) films exhibit a responsivity of ~ 0.08 mA/W and good detectivity of $\sim 63.5 \times 10^{10}$ Jones at a voltage bias of 0 V. These findings pave the way for lead-free, highly stable, and self-biased photodetectors based on $Cs_2AgIn_xBi_{1-x}Cl_6$ double perovskites.

Supporting Information

The supporting information includes the following Figures and Tables: **Figure (S1**) (a) W-H plot for $Cs_2AgIn_xBi_{(1-x)}Cl_6$; x= 0.0 sample (b) W-H plot for $Cs_2AgIn_xBi_{(1-x)}Cl_6$; x= 0.25 sample (c) W-H plot for $Cs_2AgIn_xBi_{(1-x)}Cl_6$; x=0.50 sample (d) W-H plot for $Cs_2AgIn_xBi_{(1-x)}Cl_6$; x=0.75 sample (e) W-H plot for $Cs_2AgIn_xBi_{(1-x)}Cl_6$; x=0.90 sample (c) W-H plot for $Cs_2AgIn_xBi_{(1-x)}Cl_6$; x=1 sample. **Figure (S2)** (a) TEM image and (b) histogram of $Cs_2AgIn_xBi_{(1-xa)}Cl_6$ (x = 0), (c) TEM image and (d) histogram of $Cs_2AgIn_xBi_{(1-x)}Cl_6$ (x = 1). **Figure (S3)** (a,b,c) HR-TEM images for $Cs_2AgIn_xBi_{(1-x)}Cl_6$ (x = 0.0, x = 0.50, and x=0.75) samples, respectively. (d,e,f) SAED patterns for $Cs_2AgIn_xBi_{(1-x)}Cl_6$ (x=0.0, x=0.50 and x=0.75 samples) respectively. **Figure (S4)** FE-SEM images for $Cs_2AgIn_xBi_{(1-x)}Cl_6$ (x=0.50 (a), x =0.75 (b), x=0.90 (c), and x=1.0 (d), respectively, at 200 nm scale. **Figure (S5)** EDS spectra for the synthesized samples in the energy range 0-15 keV. **Figure (S6-S10)** Elemental mapping for $Cs_2AgIn_xBi_{(1-x)}Cl_6$ (x = 0.0, x=0.50, x=0.75, x=0.90 and x=1.0 samples respectively. **Figure (S11)** (a1-a5) Core level XPS spectra of $Cs_2AgIn_xBi_{(1-x)}Cl_6$ (x=0.1) sample. (b1-b5) Core level XPS spectra of the x=25 sample. (c1-c5) Core level XPS spectra of $Cs_2AgIn_xBi_{(1-x)}Cl_6$ (x=0.9) sample. **Figure (S12)** (a1-a5**)** Survey scan XPS spectra of $Cs_2AgIn_xBi_{(1-x)}Cl_6$ (x =0.10, x = 0.25, x = 0.50, x = 0.75 and x = 0.90) samples, respectively. (b1) Survey scan XPS spectra of $Cs_2AgIn_xBi_{(1-x)}Cl6$ (x=1) sample. (b2-b5) Core level XPS spectra of x100. **Figure (S13)** Pseudo-absorption spectra of $Cs_2AgIn_xBi_{(1-x)}Cl_6$. **Figure (S14)** Fitted TRPL curves; **Figure (S15)** Comparison of optical and electrochemical band gaps estimated from UV and CV,

View Article Online
DOI: 10.1039/D5CP02259B

respectively. **Figures (S16)** (a), (b), and (c) are the TDPL spectra of $Cs_2AgIn_xBi_{(1-x)}Cl_6$ recorded in the temperature range 80K – 300 K. (x=0.25, x=0.5 and x=1.0 sample, respectively) (d), (e) and (f) are the corrected intensity vs inverse temperature graphs fitted using an Arrhenius function for (x=0.25, x=0.5 and x=1.0) samples respectively. (g), (h), and (i) are the $(FWHM)^2$ vs 1/T graphs for (x = 0.25, x = 0.50, and x=1.0), respectively. **Figure (S17)** (a-c) Deconvoluted temperature-dependent photoluminescence (TDPL) spectra of $Cs_2AgIn_xBi_{(1-x)}Cl_6$ (x = 0) at different temperatures. (d-f) Deconvoluted TDPL spectra of $Cs_2AgIn_xBi_{(1-x)}Cl_6$ (x = 0.75) at different temperatures. (g-i) Deconvoluted TDPL spectra of $Cs_2AgIn_xBi_{(1-x)}Cl_6$ (x = 0.9) at different temperatures. **Figure (S18)** (a) Photoluminescence excitation (PLE) spectrum of x = 0 sample (b and c) are the photoluminescence excitation (PLE) spectra for the x = 0.75 sample corresponding to emission at violet and yellow regions, respectively. (d and e) are the photoluminescence excitation (PLE) spectra for the x = 0.90 sample corresponding to emission at the violet and orange regions, respectively. (f) is the low temperature PLE spectra for the x=1.0 sample. **Table S1.** Comparison between Structural Parameters calculated from XRD by the Scherrer and W−H analysis. **Table S2:** Optical band gap values estimated from UV-Visible diffuse reflectance spectroscopy (DRS). **Table S3**: Atomic percentage of elements calculated from EDS analysis. **Table S4**: TRPL traces recorded for emission in the violet/blue region for x=0.75 and x=0.90 samples, respectively. **Table S5**: The values of an activation energy E_a, Huang-Rhys parameter S, Phonon energy, etc, and the corresponding values of R^2 obtained from fitted curves. **Table S6:** Photo response parameters calculated for the $Cs_2AgIn_xBi_{(1-x)}Cl_6$ (x = 0.0, 0.9, 1.0) - based photodetectors under white light illumination. **Table S7:** Summary of the reported device architectures and the important parameters of perovskite photodetectors, comparing our results with representative values reported for lead halide perovskites and other DPs in recent literature.

Acknowledgments

SNR expresses gratitude to the Chhatrapati Shahu Maharaj Research Training and Human Development Institute (SARTHI) for their generous financial assistance. GKR acknowledges Manipal Academy of Higher Education for providing Dr. TMA Pai Scholarship. MPN is grateful for the Seed Money scheme offered by Reva University. YJ is thankful to the BacPlex Technologies Private Limited, AIC Seed Foundation, Indian Institute of Science Education and Research (IISER) Pune for providing the laboratory facilities. NYD acknowledges the U.S.

View Article Online
DOI: 10.1039/D5CP02259B

Department of Energy funding (DE-SC0025350) and the Penn State Institute for Computational and Data Sciences (ICDS) seed grant support. The computational aspects of this research are carried out utilizing the computing resources of the Roar supercomputer at the Institute for Computational and Data Sciences, Pennsylvania State University.

References

(1) Jodlowski, A. D.; Roldán-Carmona, C.; Grancini, G.; Salado, M.; Ralaiarisoa, M.; Ahmad, S.; Koch, N.; Camacho, L.; de Miguel, G.; Nazeeruddin, M. K. Large Guanidinium Cation Mixed with Methylammonium in Lead Iodide Perovskites for 19% Efficient Solar Cells. *Nat. Energy* **2017**, *2* (12), 972–979. https://doi.org/10.1038/s41560-017-0054-3.

(2) Li, G.; Rivarola, F. W. R.; Davis, N. J. L. K.; Bai, S.; Jellicoe, T. C.; de la Peña, F.; Hou, S.; Ducati, C.; Gao, F.; Friend, R. H.; Greenham, N. C.; Tan, Z. Highly Efficient Perovskite Nanocrystal Light-Emitting Diodes Enabled by a Universal Crosslinking Method. *Adv. Mater.* **2016**, *28* (18), 3528–3534. https://doi.org/10.1002/adma.201600064.

(3) Gao, Y.; Huang, C.; Hao, C.; Sun, S.; Zhang, L.; Zhang, C.; Duan, Z.; Wang, K.; Jin, Z.; Zhang, N.; Kildishev, A. V.; Qiu, C.-W.; Song, Q.; Xiao, S. Lead Halide Perovskite Nanostructures for Dynamic Color Display. *ACS Nano* **2018**, *12* (9), 8847–8854. https://doi.org/10.1021/acsnano.8b02425.

(4) Amgar, D.; Stern, A.; Rotem, D.; Porath, D.; Etgar, L. Tunable Length and Optical Properties of CsPbX 3 (X = Cl, Br, I) Nanowires with a Few Unit Cells. *Nano Lett.* **2017**, *17* (2), 1007–1013. https://doi.org/10.1021/acs.nanolett.6b04381.

(5) Lin, J.; Gomez, L.; de Weerd, C.; Fujiwara, Y.; Gregorkiewicz, T.; Suenaga, K. Direct Observation of Band Structure Modifications in Nanocrystals of CsPbBr 3 Perovskite. *Nano Lett.* **2016**, *16* (11), 7198–7202. https://doi.org/10.1021/acs.nanolett.6b03552.

(6) Zhou, J.; Rong, X.; Molokeev, M. S.; Zhang, X.; Xia, Z. Exploring the Transposition Effects on the Electronic and Optical Properties of Cs 2 AgSbCl 6 via a Combined Computational-Experimental Approach. *J. Mater. Chem. A* **2018**, *6* (5), 2346–2352. https://doi.org/10.1039/C7TA10062K.

(7) De Roo, J.; Ibáñez, M.; Geiregat, P.; Nedelcu, G.; Walravens, W.; Maes, J.; Martins, J. C.; Van Driessche, I.; Kovalenko, M. V.; Hens, Z. Highly Dynamic Ligand Binding and Light Absorption Coefficient of Cesium Lead Bromide Perovskite Nanocrystals. *ACS Nano* **2016**, *10* (2), 2071–2081. https://doi.org/10.1021/acsnano.5b06295.

(8) Braly, I. L.; DeQuilettes, D. W.; Pazos-Outón, L. M.; Burke, S.; Ziffer, M. E.; Ginger, D. S.; Hillhouse, H. W. Hybrid Perovskite Films Approaching the Radiative Limit with over 90% Photoluminescence Quantum Efficiency. *Nat. Photonics* **2018**, *12* (6), 355–361. https://doi.org/10.1038/s41566-018-0154-z.

(9) Nedelcu, G.; Protesescu, L.; Yakunin, S.; Bodnarchuk, M. I.; Grotevent, M. J.; Kovalenko, M. V. Fast Anion-Exchange in Highly Luminescent Nanocrystals of Cesium Lead Halide Perovskites (CsPbX 3 , X = Cl, Br, I). *Nano Lett.* **2015**, *15* (8), 5635–5640. https://doi.org/10.1021/acs.nanolett.5b02404.

(10) Du, K.; Meng, W.; Wang, X.; Yan, Y.; Mitzi, D. B. Bandgap Engineering of Lead-Free Double Perovskite Cs 2 AgBiBr 6 through Trivalent Metal Alloying. *Angew. Chemie Int. Ed.* **2017**, *56* (28), 8158–8162. https://doi.org/10.1002/anie.201703970.

(11) Bi, Y.; Hutter, E. M.; Fang, Y.; Dong, Q.; Huang, J.; Savenije, T. J. Charge Carrier Lifetimes Exceeding 15 Ms in Methylammonium Lead Iodide Single Crystals. *J. Phys. Chem. Lett.* **2016**, *7* (5), 923–928. https://doi.org/10.1021/acs.jpclett.6b00269.

(12) Dong, Q.; Fang, Y.; Shao, Y.; Mulligan, P.; Qiu, J.; Cao, L.; Huang, J. Electron-Hole Diffusion Lengths > 175 Mm in Solution-Grown CH 3 NH 3 PbI 3 Single Crystals. *Science (80-.).* **2015**, *347* (6225), 967–970. https://doi.org/10.1126/science.aaa5760.

(13) Etgar, L. The Merit of Perovskite's Dimensionality; Can This Replace the 3D Halide Perovskite? *Energy Environ. Sci.* **2018**, *11* (2), 234–242. https://doi.org/10.1039/C7EE03397D.

(14) Wang, F.; Jiang, X.; Chen, H.; Shang, Y.; Liu, H.; Wei, J.; Zhou, W.; He, H.; Liu, W.; Ning, Z. 2D-Quasi-2D-3D Hierarchy Structure for Tin Perovskite Solar Cells with Enhanced Efficiency and Stability. *Joule* **2018**, *2* (12), 2732–2743. https://doi.org/10.1016/j.joule.2018.09.012.

(15) Krishna, A.; Gottis, S.; Nazeeruddin, M. K.; Sauvage, F. Mixed Dimensional 2D/3D Hybrid Perovskite Absorbers: The Future of Perovskite Solar Cells? *Adv. Funct. Mater.* **2019**, *29* (8). https://doi.org/10.1002/adfm.201806482.

(16) Murtaza GH, Ahmad I. First principle study of the structural and optoelectronic properties of cubic perovskites CsPbM3 (M= Cl, Br, I). Physica B: Condensed Matter. 2011 ;406(17):3222-3229, https://doi.org/10.1016/j.physb.2011.05.028

(17) Yakunin S, Protesescu L, Krieg F, Bodnarchuk MI, Nedelcu G, Humer M, De Luca G, Fiebig M, Heiss W, Kovalenko MV. Low-threshold amplified spontaneous emission and lasing from colloidal nanocrystals of caesium lead halide perovskites. Nature communications. 2015; 6(1):8056, DOI: 10.1038/ncomms9056

(18) Loredana Protesescu, Sergii Yakunin,Maryna I. Bodnarchuk, Franziska Krieg, Riccarda Caputo, Christopher H. Hendon, Ruo Xi Yang, Aron Walsh, Maksym V. Kovalenko, Nanocrystals of Cesium Lead Halide Perovskites ($CsPbX_3$, X = Cl, Br, and I): Novel Optoelectronic Materials Showing Bright Emission with Wide Color Gamut, *Nano Lett.* 2015, 15, 6, 3692–3696, https://doi.org/10.1021/nl5048779

(19) Hutter, E. M.; Gélvez-Rueda, M. C.; Osherov, A.; Bulović, V.; Grozema, F. C.; Stranks, S. D.; Savenije, T. J. Direct–Indirect Character of the Bandgap in Methylammonium Lead Iodide Perovskite. *Nat. Mater.* **2017**, *16* (1), 115–120. https://doi.org/10.1038/nmat4765.

(20) Park, B.; Philippe, B.; Zhang, X.; Rensmo, H.; Boschloo, G.; Johansson, E. M. J. Bismuth Based Hybrid Perovskites A 3 Bi 2 I 9 (A: Methylammonium or Cesium) for Solar Cell Application. *Adv. Mater.* **2015**, *27* (43), 6806–6813. https://doi.org/10.1002/adma.201501978.

(21) Hebig, J.-C.; Kühn, I.; Flohre, J.; Kirchartz, T. Optoelectronic Properties of (CH 3 NH 3) 3 Sb 2 I 9 Thin Films for Photovoltaic Applications. *ACS Energy Lett.* **2016**, *1* (1), 309–314. https://doi.org/10.1021/acsenergylett.6b00170.

(22) Slavney, A. H.; Hu, T.; Lindenberg, A. M.; Karunadasa, H. I. A Bismuth-Halide Double Perovskite with Long Carrier Recombination Lifetime for Photovoltaic Applications. *J. Am. Chem. Soc.* **2016**, *138* (7), 2138–2141. https://doi.org/10.1021/jacs.5b13294.

(23) McClure, E. T.; Ball, M. R.; Windl, W.; Woodward, P. M. Cs 2 AgBiX 6 (X = Br, Cl): New Visible Light Absorbing, Lead-Free Halide Perovskite Semiconductors. *Chem. Mater.* **2016**, *28* (5), 1348–1354. https://doi.org/10.1021/acs.chemmater.5b04231.

(24) Leng, M.; Chen, Z.; Yang, Y.; Li, Z.; Zeng, K.; Li, K.; Niu, G.; He, Y.; Zhou, Q.; Tang, J. Lead-Free, Blue Emitting Bismuth Halide Perovskite Quantum Dots. *Angew. Chemie Int. Ed.* **2016**, *55* (48), 15012–15016. https://doi.org/10.1002/anie.201608160.

View Article Online
DOI: 10.1039/D5CP02259B

(25) Yang, B.; Chen, J.; Hong, F.; Mao, X.; Zheng, K.; Yang, S.; Li, Y.; Pullerits, T.; Deng, W.; Han, K. Lead-Free, Air-Stable All-Inorganic Cesium Bismuth Halide Perovskite Nanocrystals. *Angew. Chemie Int. Ed.* **2017**, *56* (41), 12471–12475. https://doi.org/10.1002/anie.201704739.

(26) Zhang, J.; Yang, Y.; Deng, H.; Farooq, U.; Yang, X.; Khan, J.; Tang, J.; Song, H. High Quantum Yield Blue Emission from Lead-Free Inorganic Antimony Halide Perovskite Colloidal Quantum Dots. *ACS Nano* **2017**, *11* (9), 9294–9302. https://doi.org/10.1021/acsnano.7b04683.

(27) Zhang, Y.; Yin, J.; Parida, M. R.; Ahmed, G. H.; Pan, J.; Bakr, O. M.; Brédas, J.-L.; Mohammed, O. F. Direct-Indirect Nature of the Bandgap in Lead-Free Perovskite Nanocrystals. *J. Phys. Chem. Lett.* **2017**, *8* (14), 3173–3177. https://doi.org/10.1021/acs.jpclett.7b01381.

(28) Yang, B.; Chen, J.; Yang, S.; Hong, F.; Sun, L.; Han, P.; Pullerits, T.; Deng, W.; Han, K. Lead-Free Silver-Bismuth Halide Double Perovskite Nanocrystals. *Angew. Chemie Int. Ed.* **2018**, *57* (19), 5359–5363. https://doi.org/10.1002/anie.201800660.

(29) Creutz, S. E.; Crites, E. N.; De Siena, M. C.; Gamelin, D. R. Colloidal Nanocrystals of Lead-Free Double-Perovskite (Elpasolite) Semiconductors: Synthesis and Anion Exchange To Access New Materials. *Nano Lett.* **2018**, *18* (2), 1118–1123. https://doi.org/10.1021/acs.nanolett.7b04659.

(30) Bekenstein, Y.; Dahl, J. C.; Huang, J.; Osowiecki, W. T.; Swabeck, J. K.; Chan, E. M.; Yang, P.; Alivisatos, A. P. The Making and Breaking of Lead-Free Double Perovskite Nanocrystals of Cesium Silver–Bismuth Halide Compositions. *Nano Lett.* **2018**, *18* (6), 3502–3508. https://doi.org/10.1021/acs.nanolett.8b00560.

(31) Luo, J.; Li, S.; Wu, H.; Zhou, Y.; Li, Y.; Liu, J.; Li, J.; Li, K.; Yi, F.; Niu, G.; Tang, J. Cs 2 AgInCl 6 Double Perovskite Single Crystals: Parity Forbidden Transitions and Their Application For Sensitive and Fast UV Photodetectors. *ACS Photonics* **2018**, *5* (2), 398–405. https://doi.org/10.1021/acsphotonics.7b00837.

(32) Volonakis, G.; Haghighirad, A. A.; Milot, R. L.; Sio, W. H.; Filip, M. R.; Wenger, B.; Johnston, M. B.; Herz, L. M.; Snaith, H. J.; Giustino, F. Cs 2 InAgCl 6 : A New Lead-Free Halide Double Perovskite with Direct Band Gap. *J. Phys. Chem. Lett.* **2017**, *8* (4), 772–778. https://doi.org/10.1021/acs.jpclett.6b02682.

(33) Yang, B.; Mao, X.; Hong, F.; Meng, W.; Tang, Y.; Xia, X.; Yang, S.; Deng, W.; Han, K. Lead-Free Direct Band Gap Double-Perovskite Nanocrystals with Bright Dual-Color Emission. *J. Am. Chem. Soc.* **2018**, *140* (49), 17001–17006. https://doi.org/10.1021/jacs.8b07424.

(34) Locardi, F.; Cirignano, M.; Baranov, D.; Dang, Z.; Prato, M.; Drago, F.; Ferretti, M.; Pinchetti, V.; Fanciulli, M.; Brovelli, S.; De Trizio, L.; Manna, L. Colloidal Synthesis of Double Perovskite Cs 2 AgInCl 6 and Mn-Doped Cs 2 AgInCl 6 Nanocrystals. *J. Am. Chem. Soc.* **2018**, *140* (40), 12989–12995. https://doi.org/10.1021/jacs.8b07983.

(35) Zhang, P.; Yang, J.; Wei, S.-H. Manipulation of Cation Combinations and Configurations of Halide Double Perovskites for Solar Cell Absorbers. *J. Mater. Chem. A* **2018**, *6* (4), 1809–1815. https://doi.org/10.1039/C7TA09713A.

(36) Luo, J.; Wang, X.; Li, S.; Liu, J.; Guo, Y.; Niu, G.; Yao, L.; Fu, Y.; Gao, L.; Dong, Q.; Zhao, C.; Leng, M.; Ma, F.; Liang, W.; Wang, L.; Jin, S.; Han, J.; Zhang, L.; Etheridge, J.; Wang, J.; Yan, Y.; Sargent, E. H.; Tang, J. Efficient and Stable Emission of Warm-White Light from Lead-Free Halide Double Perovskites. *Nature* **2018**, *563* (7732), 541–545. https://doi.org/10.1038/s41586-018-0691-0.

(37) Zhao, X.-G.; Yang, D.; Ren, J.-C.; Sun, Y.; Xiao, Z.; Zhang, L. Rational Design of Halide Double Perovskites for Optoelectronic Applications. *Joule* **2018**, *2* (9), 1662–1673.

https://doi.org/10.1016/j.joule.2018.06.017.

(38) Ravi, V. K.; Singhal, N.; Nag, A. Initiation and Future Prospects of Colloidal Metal Halide Double-Perovskite Nanocrystals: Cs 2 AgBiX 6 (X = Cl, Br, I). *J. Mater. Chem. A* **2018**, *6* (44), 21666–21675. https://doi.org/10.1039/C8TA06126B.

(39) Rahane, S. N.; Rahane, G. K.; Mandal, A.; Jadhav, Y.; Godha, A.; Rokade, A.; Shah, S.; Hase, Y.; Waghmare, A.; Saykar, N. G.; Roy, A.; Salgaonkar, K. N.; Dubal, D.; Makineni, S. K.; Dzade, N. Y.; Jadkar, S. R.; Rondiya, S. R. Lead-Free Cs 2 AgBiCl 6 Double Perovskite: Experimental and Theoretical Insights into the Self-Trapping for Optoelectronic Applications. *ACS Phys. Chem. Au* **2024**, *4* (5), 476–489. https://doi.org/10.1021/acsphyschemau.4c00008.

(40) Barma, S. V.; Jathar, S. B.; Huang, Y.-T.; Jadhav, Y. A.; Rahane, G. K.; Rokade, A. V.; Nasane, M. P.; Rahane, S. N.; Cross, R. W.; Suryawanshi, M. P.; Jo, S. B.; Hoye, R. L. Z.; Jadkar, S. R.; Dzade, N. Y.; Rondiya, S. R. Synthesis and Interface Engineering in Heterojunctions of Tin-Selenide-Based Nanostructures for Photoelectrochemical Water Splitting. *ACS Appl. Nano Mater.* **2024**, *7* (2), 1986–1999. https://doi.org/10.1021/acsanm.3c05202.

(41) Deshpande, S. S.; Saykar, N. G.; Mandal, A.; Rahane, S.; Jadhav, Y. A.; Upadhyay Kahaly, M.; Nagy, G. N.; Shinde, A.; Suresh, S.; Rondiya, S. R. Unravelling Structural, Optical, and Band Alignment Properties of Mixed Pb–Sn Metal-Halide Quasi-2D Ruddlesden–Popper Perovskites. *Langmuir* **2024**, *40* (31), 16180–16189. https://doi.org/10.1021/acs.langmuir.4c01278.

(42) Jadhav, Y. A.; Thakur, P. R.; Haram, S. K. Voltammetry Investigation on Copper Zinc Tin Sulphide /Selenide (CZTSxSe1-x) Alloy Nanocrystals: Estimation of Composition Dependent Band Edge Parameters. *Sol. Energy Mater. Sol. Cells* **2016**, *155*, 273–279. https://doi.org/10.1016/j.solmat.2016.06.030.

(43) Kresse, G.; Furthmüller, J. Efficiency of Ab-Initio Total Energy Calculations for Metals and Semiconductors Using a Plane-Wave Basis Set. *Comput. Mater. Sci.* **1996**, *6* (1), 15–50. https://doi.org/10.1016/0927-0256(96)00008-0.

(44) Perdew, J. P.; Burke, K.; Ernzerhof, M. Generalized Gradient Approximation Made Simple. *Phys. Rev. Lett.* **1996**, *77* (18), 3865–3868. https://doi.org/10.1103/PhysRevLett.77.3865.

(45) Blöchl, P. E. Projector Augmented-Wave Method. *Phys. Rev. B* **1994**, *50* (24), 17953–17979. https://doi.org/10.1103/PhysRevB.50.17953.

(46) Monkhorst, H. J.; Pack, J. D. Special Points for Brillouin-Zone Integrations. *Phys. Rev. B* **1976**, *13* (12), 5188–5192. https://doi.org/10.1103/PhysRevB.13.5188.

(47) Grimme, S.; Antony, J.; Ehrlich, S.; Krieg, H. A Consistent and Accurate Ab Initio Parametrization of Density Functional Dispersion Correction (DFT-D) for the 94 Elements H-Pu. *J. Chem. Phys.* **2010**, *132* (15). https://doi.org/10.1063/1.3382344.

(48) M Ganose, A.; J Jackson, A.; O Scanlon, D. Sumo: Command-Line Tools for Plotting and Analysis of Periodic Ab Initio Calculations. *J. Open Source Softw.* **2018**, *3* (28), 717. https://doi.org/10.21105/joss.00717.

(49) Wang, V.; Xu, N.; Liu, J.-C.; Tang, G.; Geng, W.-T. VASPKIT: A User-Friendly Interface Facilitating High-Throughput Computing and Analysis Using VASP Code. *Comput. Phys. Commun.* **2021**, *267*, 108033. https://doi.org/10.1016/j.cpc.2021.108033.

(50) M. Fox, Optical properties of solids, Oxford Press, 2002, https://doi.org/10.1119/1.1691372

(51) Xiao, Z.; Du, K. Z.; Meng, W.; Wang, J.; Mitzi, D. B.; Yan, Y. Intrinsic Instability of Cs2In(I)M(III)X6 (M = Bi, Sb; X = Halogen) Double Perovskites: A Combined Density Functional Theory and Experimental Study. *J. Am. Chem. Soc.* **2017**, *139* (17), 6054– 6057, DOI: 10.1021/jacs.7b02227

View Article Online
DOI: 10.1039/D5CP02259B

(52) Jun Zhou, Zhiguo Xia, Maxim S. Molokeev, Xiuwen Zhang, Dongsheng Peng, Quanlin Liu, Composition design, optical gap and stability investigations of lead-free halide double perovskite Cs2AgInCl6, J. Mater. Chem. A, 2017, 5, 15031, DOI: 10.1039/c7ta04690a

(53) Manna, D.; Kangsabanik, J.; Das, T. K.; Das, D.; Alam, A.; Yella, A. Lattice Dynamics and Electron–Phonon Coupling in Lead-Free Cs 2 AgIn 1– x Bi x Cl 6 Double Perovskite Nanocrystals. *J. Phys. Chem. Lett.* **2020**, *11* (6), 2113–2120. https://doi.org/10.1021/acs.jpclett.0c00206.

(54) Siddique, H.; Xu, Z.; Li, X.; Saeed, S.; Liang, W.; Wang, X.; Gao, C.; Dai, R.; Wang, Z.; Zhang, Z. Anomalous Octahedron Distortion of Bi-Alloyed Cs 2 AgInCl 6 Crystal via XRD, Raman, Huang–Rhys Factor, and Photoluminescence. *J. Phys. Chem. Lett.* **2020**, *11* (22), 9572–9578. https://doi.org/10.1021/acs.jpclett.0c02852.

(55) Zeng, R.; Zhang, L.; Xue, Y.; Ke, B.; Zhao, Z.; Huang, D.; Wei, Q.; Zhou, W.; Zou, B. Highly Efficient Blue Emission from Self-Trapped Excitons in Stable Sb 3+ -Doped Cs 2 NaInCl 6 Double Perovskites. *J. Phys. Chem. Lett.* **2020**, *11* (6), 2053–2061. https://doi.org/10.1021/acs.jpclett.0c00330.

(56) Volonakis, G.; Filip, M. R.; Haghighirad, A. A.; Sakai, N.; Wenger, B.; Snaith, H. J.; Giustino, F. Lead-Free Halide Double Perovskites via Heterovalent Substitution of Noble Metals. *J. Phys. Chem. Lett.* **2016**, *7* (7), 1254–1259. https://doi.org/10.1021/acs.jpclett.6b00376.

(57) Meng, W.; Wang, X.; Xiao, Z.; Wang, J.; Mitzi, D. B.; Yan, Y. Parity-Forbidden Transitions and Their Impact on the Optical Absorption Properties of Lead-Free Metal Halide Perovskites and Double Perovskites. *J. Phys. Chem. Lett.* **2017**, *8* (13), 2999–3007. https://doi.org/10.1021/acs.jpclett.7b01042.

(58) Inamdar, S. N.; Ingole, P. P.; Haram, S. K. Determination of Band Structure Parameters and the Quasi-Particle Gap of CdSe Quantum Dots by Cyclic Voltammetry. *ChemPhysChem* **2008**, *9* (17), 2574–2579. https://doi.org/10.1002/cphc.200800482.

(59) Wadhai, S.; Jadhav, Y.; Thakur, P. Synthesis of Metal-Free Phosphorus Doped Graphitic Carbon Nitride-P25 (TiO2) Composite: Characterization, Cyclic Voltammetry and Photocatalytic Hydrogen Evolution. *Sol. Energy Mater. Sol. Cells* **2021**, *223*, 110958. https://doi.org/10.1016/j.solmat.2021.110958.

(60) Kannan, P. K.; Late, D. J.; Morgan, H.; Rout, C. S. Recent developments in 2D layered inorganic nanomaterials for sensing. *Nanoscale* **2015**, *7*, 13293– 13312, DOI: 10.1039/C5NR03633J

(61) Dou, L.; Yang, Y. M.; You, J.; Hong, Z.; Chang, W.-H.; Li, G.; Yang, Y. Solution-processed hybrid perovskite photodetectors with high detectivity. *Nat. Commun.* **2014**, *5*, 5404, DOI: 10.1038/ncomms6404

AUTHOR INFORMATION

Corresponding Authors

Nelson Y. Dzade*

Sandesh R. Jadkar*

Present Addresses

Nelson Y. Dzade*

View Article Online
DOI: 10.1039/D5CP02259B

Department of Energy and Mineral Engineering, Pennsylvania State University, University Park, PA 16802, United States.

Sandesh R. Jadkar*

Department of Physics, Savitribai Phule Pune University, Pune 411007, India.

View Article Online
DOI: 10.1039/D5CP02259B

Data Availability Statement

The authors confirm that the data supporting the findings of this study are available within the article [and/or] its supplementary materials. The raw data is available on request from the corresponding author - NYD.